

Application of Deep Learning Methods for Distinguishing Gamma-Ray Bursts from Fermi/GBM TTE Data

PENG ZHANG (张鹏) ,^{1,2} BING LI (李兵) ,^{2,3,4} RENZHOU GUI (桂任舟),¹ SHAOLIN XIONG (熊少林),² ZE-CHENG ZOU (邹泽城) ,³ XIANGGAO WANG (王祥高),⁴ XIAOBO LI (李小波),² CE CAI (蔡策),⁵ YI ZHAO (赵一),⁶ YANQIU ZHANG (张艳秋) ,² WANGCHEN XUE (薛王陈),² CHAO ZHENG (郑超),² AND HONGYU ZHAO (赵宏宇)⁷

¹College of Electronic and Information Engineering, Tongji University, Shanghai 201804, China

²Key Laboratory of Particle Astrophysics, Chinese Academy of Sciences, Beijing 100049, China, libing@ihep.ac.cn, rzgui@tongji.edu.cn

³School of Astronomy and Space Science, Nanjing University, Nanjing 210023, China

⁴Guangxi Key Laboratory for Relativistic Astrophysics, Nanning 530004, China

⁵College of Physics and Hebei Key Laboratory of Photophysics Research and Application, Hebei Normal University, Shijiazhuang, Hebei 050024, China

⁶School of Computer and Information, Dezhou University, Dezhou 253023, China

⁷School of Computing and Artificial Intelligence, Southwest Jiaotong University, Chengdu 611756, China

ABSTRACT

To investigate GRBs in depth, it is crucial to develop an effective method for identifying GRBs accurately. Current criteria, e.g., onboard blind search, ground blind search, and target search, are limited by manually set thresholds and perhaps miss GRBs, especially for sub-threshold events. We proposed a novel approach that utilizes convolutional neural networks (CNNs) to distinguish GRBs and non-GRBs directly. We structured three CNN models, *plain*-CNN, ResNet, and ResNet-CBAM, and endeavored to exercise fusing strategy models. Count maps of NaI detectors onboard Fermi/GBM were employed as the input samples of datasets and models were implemented to evaluate their performance on different time scale data. The ResNet-CBAM model trained on 64 ms dataset achieves high accuracy overall, which includes residual and attention mechanism modules. The visualization methods of Grad-CAM and t-SNE explicitly displayed that the optimal model focuses on the key features of GRBs precisely. The model was applied to analyze one-year data, accurately identifying approximately 98% of GRBs listed in the Fermi burst catalog, 8 out of 9 sub-threshold GRBs, and 5 GRBs triggered by other satellites, which demonstrated the deep learning methods could effectively distinguish GRBs from observational data. Besides, thousands of unknown candidates were retrieved and compared with the bursts of SGR J1935+2154 for instance, which exemplified the potential scientific value of these candidates indeed. Detailed studies on integrating our model into real-time analysis pipelines thus may improve their accuracy of inspection, and provide valuable guidance for rapid follow-up observations of multi-band telescopes.

Keywords: Gamma-ray astronomy (628), Gamma-ray bursts (629), High energy astrophysics (739), Convolutional neural networks (1938), Dimensionality reduction(1943), Astronomy data analysis (1858)

1. INTRODUCTION

Gamma-ray bursts (GRBs) are the brightest explosions from distant galaxies, releasing isotropic energies up to 10^{54} ergs in gamma-rays of prompt emission (e.g. Atteia et al. 2017; Minaev & Pozanenko 2020), typically peaking in $10\text{--}10^4$ keV energy band (Gruber et al. 2014; Preece et al. 2016; Ohmori et al. 2019), and mostly exhibiting a non-thermal spectrum (Band et al. 1993; Wang et al. 2020), showing intricately irregular pulses from less than a second to tens of thousands seconds. GRBs are generally separated into two classes, long duration GRBs and short duration GRBs (Kouveliotou et al. 1993). A large number of observations have supported the theoretical predictions that long duration GRBs are produced by collapsing massive stars and at least some short duration GRBs originate from binary neutron star mergers (for reviews see Kumar & Zhang 2015; Mészáros 2019). Still, there are many unsolved mysteries about the origin of GRBs.

The rapid identification of the GRBs by the space telescope is conducive to guide other telescopes for joint or follow-up observations. Multi-band follow-up observations are crucial to researching the afterglow, host galaxies, and other information of GRBs. However, the light curve morphology of GRBs is extremely complex, especially the main episode known as the prompt emission phase. The light curve is irregular and multi-peak, which makes it difficult to identify GRBs quickly and accurately. The onboard automatic trigger search algorithm searches triggers through the signal-to-noise ratio (SNR) of the peak in the light curve, identical to the ground blind search algorithm (Band 2002). The coherent search adopted by the target search algorithm requires the aid of additional trigger time (Blackburn et al. 2013). Abraham et al. (2019) designed a method of searching for GRBs from the morphology of the light curve. This method used a hierarchical cluster algorithm to find candidates, and then compared the light curve of these candidates with the typical GRBs in the template bank. However, the above methods highly depend on the SNR of the event pulses on the detected light curve, which requires manual participation. It would miss some weak and inconspicuous events, such as sub-threshold bursts¹.

In recent years, machine learning (ML) has begun to play a powerful role in various fields. ML provides a useful complement to the common paradigm of model-driven data analysis through a data-driven approach. The intersection of ML and astronomy is a fairly new paradigm that trains artificial intelligence systems on huge amounts of archival data to produce high quality results for extracting domain knowledge and facilitating new discoveries (for review see Baron 2019; Sen et al. 2022; Kembhavi & Pattnaik 2022). As a sub-field of machine learning, deep learning (DL) excels in discovering effective representations of internal patterns and correlations from massive amounts of data automatically. DL methods have made great success in computer vision and natural language processing, and there are many applications in astronomy and astrophysics (Goode et al. 2022; De et al. 2022; Venn et al. 2019). Deep learning uses computational model consist of multiple processing layers to learn data representations at the abstraction level (Lecun et al. 2015). Convolutional neural network (CNN) is a commonly used deep learning algorithm that automatically extracts features from high-dimensional data. The CNN is useful for image classification because it learns the underlying features of samples layer by layer and retains the spatial relations between pixels. Recently, deep learning has been developing rapidly and gained widespread attention and application in the field of astronomy and astrophysics, and shown a growing trend in hot topics of astronomy research. A large number of research efforts have been made for digging knowledge depth from huge amounts of observation data, e.g., gravitational wave detection (Qiu et al. 2023a), gravitational lensing identification (Hezaveh et al. 2017), exoplanet search (Kumari et al. 2023), transient source classification (Agarwal et al. 2020), solar flare prediction (Zheng et al. 2023), background estimation (Crupi et al. 2023), etc. The image classification problems puzzled astronomers for a long time, CNN algorithms are a type of neural network that bring us closer to understanding the intrinsic characteristics within abundant images. Hezaveh et al. (2017) described a CNN technology to perform fast and automated gravitational lens analyses. Moreover, relying on the quality of the dataset, recent studies have shown that CNN methods could be used for inferring galaxy cluster masses directly from mock images and galaxy member dynamics rather than on any other assumptions. de Andres et al. (2022) applied the CNNs that trained by using simulated intensity maps to predict the galaxy cluster masses from the real Planck maps, and obtained an results overall in agreement with masses that estimated by Planck and determine. The signal search of bursts is another puzzling problems in time domain astronomy, and the CNNs are used to analyze data in several contexts. Jia et al. (2023) used the object detection method to detect celestial objects candidates of from the image with photon flux distribution, which achieves over 90% completeness for targets. Yang et al. (2021) attempted to apply an algorithm based on ResNet to search for weak Fast radio bursts from the data archive of four years observations of Parkes radio telescope. Finally, 81 new candidates that were difficult to discover manually were identified. Parmiggiani et al. (2021) presented a CNN approach for detecting GRBs by classifying the AGILE-GRID intensity maps database, the GRB detection capability was improved dramatically. Overall, large amounts and high quality observed or simulated data were used to train and validate CNN models which achieved impressive results. Parmiggiani et al. (2023) applied the CNN auto-encoder to reconstruct the background-only light curves, and the GRBs were searched by reconstruction error exceeding the threshold. This method recovered 72 GRBs which are not present in AGILE catalog and was implemented in real-time analysis pipeline. Astronomy is rich with full raw information within time series data and image-based types of data that are well suited to analysis via CNNs in

¹ Note that sub-threshold GRBs are critical to GW/GRB association, e.g., GBM-190816 is suggested to be possibly associated with a sub-threshold GW event (Yang et al. 2020; Goldstein et al. 2019).

particular. Large amounts and high quality observed or simulated data were used to train and validate CNN models that impressive results were achieved as due to their extensive employ.

Until January 2022, the Fermi Gamma-ray Burst Monitor (GBM) has detected over 3200 GRBs. Such a large amount of data allows us to directly use the observed real GRBs to train the deep learning model. Furthermore, the dimensionality reduction method is utilized to visually analyze the distribution differences among the various types of detected GRBs. The dimensionality reduction method transforms the raw data from a high-dimensional space to a low-dimensional space, enabling easier visualization and evaluation. [Jespersen et al. \(2020\)](#) employed the dimensionality reduction method of t-distributed Stochastic Neighbor Embedding (t-SNE) to achieve clear separation between short bursts and long bursts from the light curves of the Swift/BAT satellite. [Steinhardt et al. \(2023\)](#) utilized the t-SNE method to analyze the data from three GRB satellites and discovered uncommon types of GRBs in addition to the long and short bursts.

Inspired by the above research, we design an image classification method by CNN to distinguish GRBs. Based on observations from Fermi/GBM spanning over 13 years, we construct a training set, validation set, and test set, as described in Section 2. Section 3 presents the structure of three models and their training procedures. Additionally, we introduce analysis methods for feature visualization (Grad-CAM) and dimensionality reduction visualization (t-SNE). Section 4 shows the test results of each model and demonstrates the application of the optimal model in identifying GRBs from one year of Fermi data. Section 5 discusses the performance and practical application effects of the model, and presents the conclusion.

2. DATA SET

For training our deep learning models, we need to build the data set that consist of GRB category and non-GRB category. The NaI detectors of GBM on board the Fermi telescope have detected 3083 GRBs to the end of June 2021. The Time-Tagged Event (TTE) format data of these GRBs has been published online². We download all of the GRBs data, which contains the data of all triggered detectors for each GRB. In order to generate the samples of the GRB category, the data needs to be filtered. In Fermi GRBs area, the distribution of T_{90} is researched ([Von Kienlin et al. 2020](#)). Over 90% GRBs are less than 100 seconds. The entire burst sample are needed, accordingly the data should include the burst phase and the background before and after the burst. For the Fermi/GBM detected GRBs, its published burst TTE data overlaps the whole T_{90} period of each GRB event and covers from roughly 20 s pre-trigger to 300 s post-trigger. Considering computing efficiency and performance of the deep learning models, we take a 120 seconds length for each GRB sample, which contained the complete burst period and the background for at least 10 seconds before and after the burst event. There are only about 3000 GRBs left, which seems to be a tiny data set for training deep learning model. Each GRB event was detected by multiple NaI detectors of Fermi/GBM, and each event appears slight differences in different detectors due to the direction and response of the NaI detectors. Consequently the event that triggered by each single detector would be recognized as an individual GRB event. It is possible to multiply the number of GRB samples. We take the signal of each trigger detector as an independent GRB sample. Finally, we obtain 6330 GRB samples which might be a sufficient GRB set for training and testing.

We mainly use the daily data of Fermi/GBM for building the non-GRB set. All the Fermi/GBM daily observations are also published³ in TTE format. We should ensure the data do not include the GRBs. The daily data products are composed of all GBM detector observations continuously in hour, regardless of whether a burst occurred. We download a number of daily data products after filtering out the burst TTE data of Fermi GRBs. We randomly choose the time and ID of NaI detectors to produce non-GRB data. A total of 4000 daily TTE files that do contain the time period of GRBs were downloaded. Sequentially, 10 segments of non-overlapping 120 seconds long data are extracted from each choosing data, and 40000 non-GRB events are obtained in total. All these non-GRB events are divided into three sets according to time. It is important to maintain the quantitative balance between the sample categories. Each of the three sets is randomly arranged, and we randomly select 10000 non-GRB events as non-GRB samples.

The count maps of GRBs contain essential information about their physical features and emission mechanisms, see Figure 1. Both GRB samples and non-GRB samples are composed of total 128 channel data covering energies from 8 keV to 2 MeV. Notice that we do not use the detector response function to convert channel to energy. The count rate data of the whole samples are not corrected by dead time. There exist a significant variety of burst signals between

² <https://heasarc.gsfc.nasa.gov/FTP/fermi/data/gbm/burst/>

³ <https://heasarc.gsfc.nasa.gov/FTP/fermi/data/gbm/daily/>

different time scales (Bhat 2013). Generally, multiple time scales of 16, 32, 64, 128, and 256 ms are implemented in searching trigger (Von Kienlin et al. 2020; Blackburn et al. 2013). In our data pre-processing, the time scales of 256, 128, and 64 ms are respectively adopted. To eliminate the magnitude difference between samples, each count map is individually normalized. It's worth noting that we used a method known as min-max normalization in this procedure to normalize the data values of counts in each count-map. Each count value was converted to a value between 0 and 1 referring to a formula: New value = (value - min) / (max - min) * 1. The three data sets of training set, validation set, and test set are essential in deep learning method. The training set is used to fit the models, and after each training epoch, the validation set is applied to verify the performance of the current model. The test set is adopted to assess generalization of the final optimal model. To avoid data confusion, we divide the samples into the above data sets based on time period, see Table 1 for detail. The ratio of the sample numbers in these three data sets is reasonable.

3. METHODS

3.1. Architecture of Neural Networks

The convolution block (Conv-block) is the base block for all the models in our work, comprising a convolutional layer, an instance normalization layer, an activation function, see Figure 2(a). We use multiple convolutional kernels of size 3×3 and of default stride 1 in the convolutional layer to extract features from input samples. The Instance Normalization layer, proposed by Ulyanov (Ulyanov et al. 2016), was utilized to normalize the feature maps, thereby constraining the convergence of the model. Nonlinear factors are incorporated into the model through the activation function to enhance its expressiveness. We adopt an effective activation function called Rectified Liner Unit (Relu) presented by Glorot et al. (2011). The advantages of the *Relu* function include addressing the vanishing gradient problem, faster computation speed, and sparse activation. This activation function is widely used in deep learning model (He et al. 2016; Woo et al. 2018).

Based on the Conv-block, we construct a general CNN model named as *plain-CNN*, as shown in Figure 2(b). The initial component of plain-CNN comprises a Conv-block with 128 convolutional kernels and a max-pooling layer, both with a stride of 2. The primary objective of setting the stride as 2 is to reduce the size of the feature map, thereby simplifying the model's complexity and enhancing computational efficiency. In the subsequent section, with the aim of extracting deeper features, we sequentially stack 4 convolutional units, each comprising three Conv-blocks, with every Conv-block containing 128 convolutional kernels. The final component of the *plain-CNN* model consists of a flatten layer, a dropout layer, and a classifier. The flatten layer sequentially flattens the features output from the fourth convolutional unit, thereby converting the multidimensional input into a one-dimensional form. We add a dropout layer which is proposed by Srivastava et al. (2014). During model training, this layer could randomly deactivate neurons with a probability of p to alleviate model overfitting, and we conservatively set p to 0.5. As the nonlinear classifier, it consists of two fully connected layers (FC) with 8 and 2 neurons, respectively. The classification results of the input samples are presented as probabilities. We employ the Softmax function to calculate the probabilities for binary classification, whose formula is

$$\text{Softmax}(z_i) = \frac{e^{z_i}}{\sum_{c=1}^C e^{z_c}}, \quad (1)$$

where z_i is the output of the classifier. i denotes the category index and the total number of categories is C .

Deep neural networks that stack a large number of convolutional layers may suffer from the degradation problem, which leads to a decrease in model performance. He et al. (2016) proposed a residual module to mitigate the degradation problem of network. The residual module establishes a shortcut (skip) connection between a shallow layer and a deep layer to achieve identical mapping, which enables the model to ignore redundant layers. The residual module also enables fast convergence in the early stages of model training, and facilitates the training of deeper networks more effectively. For solving the problem of the vanishing/exploding gradient, the residual blocks were introduced into the architecture of plain-CNN model making an extension and enhancement network model, known as the residual network (ResNet). Residual blocks were stacked together to make a ResNet which model is characterized by adding shortcut connections (+) to each convolutional unit of the second part of *plain-CNN* model, whereas other structures remain consistent with it, see Figure 2(c).

One key focus of CNN architecture design is the attention mechanism, which achieves feature selection by assigning weights to features based on their significance. Woo et al. (2018) proposed a lightweight and plug-and-play attention module, the Convolutional Block Attention Module (CBAM), which performs attentive operations jointly in spatial

and channel dimensions and separately refines feature values using spatial attention and channel attention of input features. The feature maps and attention weights are multiplied to achieve adaptive feature refinement, which significantly enhances the feature values. On the basis of ResNet model, we add a CBAM module to the end of each convolutional unit, forming the ResNet-CBAM model, see Figure 2(d). The CBAM modules were introduced into the architecture of ResNet model, enabling the model to selectively focus on critical features, enhancing the model's representational capacity and recognition performance consequently. In contrast, the *plain*-CNN and ResNet could emphasize deep feature extraction primarily, while the ResNet-CBAM further enhances the feature representation capacity of model through attention mechanisms. The ResNet-CBAM model was indeed structured to serve supplementary and augmenting components to ResNet.

3.2. Training and Optimization

3.2.1. For Single Network

The training of the original model requires the initialization of parameters for each hidden layer at the beginning. Here we set the initial parameters of all hidden layers as a truncated normal distribution which is generated by the *he_normal* (He et al. 2015). To reduce memory consumption, the training sets are divided into multiple batches to train our models. During each training epoch, only one batch of samples is input into the model, and the classification probabilities are output in turn. Both GRB set samples and non-GRB set samples are randomly shuffled and labeled with a sequence number. Then, adjacent 32 samples are grouped as a batch based on their sequence number, and any remaining samples with fewer than 32 are also used as one batch. This process is known as forward propagation. Loss function plays a crucial role in deep learning model, and it is used to guide model optimization and parameter updates. The cross-entropy loss function are commonly used for classification models (Qiu et al. 2023b; Shi et al. 2023). We choose categorical-crossentropy as the loss function to measure the discrepancy between the predicted output and the expected output. This loss function is defined as

$$\text{Loss} = - \sum_{c=1}^C y_c \cdot \log p_c \quad (2)$$

where C is total number of categories and y is the real label of the sample. p is the predicted value of the model output by the Softmax function.

The purpose of iterative training is to find the optimal parameter settings for the hidden layers in order to minimize the loss using the gradient descent algorithm. This algorithm calculates the gradient of various parameters based on the loss. The negative gradient, combined with a variable known as the learning rate, is used to update the parameters. This process is known as backward propagation. During each training epoch, every batch of samples from the training dataset goes through forward and backward propagation sequentially. We choose Adam that proposed by Kingma & Ba (2017) as the optimizer to accelerate this gradient descent. Setting a non-fixed learning rate at each stage of the iterative optimization would facilitate finding the minimum loss quickly. At the early stage, a large learning rate was set to accelerate parameter optimization, and then we gradually reduce the learning rate to search for optimal parameters. Many researches set learning rate as 0.001 for deep learning models (Parmiggiani et al. 2021; Pinchuk & Margot 2022; Merz et al. 2023). We conducted experimental tests to assess the impact of learning rates of 0.01, 0.001, and 0.0001, respectively. We set 0.001 as the initial learning rate for our models. If the training loss does not decrease after 20 consecutive epochs, we reduce the learning rate by a factor of 2 until it reaches 0.00005. The early stopping mechanism is widely adopted prevent the overfitting issue (Nevavuori et al. 2019; Stoppa et al. 2023; Ulas 2023; Wu et al. 2024). The training process would be terminated when the validation accuracy does not increase for 40 consecutive epochs. The learning curve is utilized to describe the evolving performance of a model on training data over experience or time. It assists in analyzing the training effectiveness of model, diagnosing whether the model is experiencing in overfitting issues or underfitting issues, reducing the computational complexity of model training and hyperparameter tuning, and important for the selection of an appropriate model. The parameters settings corresponding to highest validate accuracy in the training epochs are saved and adopted as our final model. Our models are implemented using Keras⁴ with the TensorFlow⁵ backend. We train ResNet-CBAM with batch size of 32 per epoch, which takes around 130 s on a computer with one GPU (NVIDIA GTX-1080Ti).

⁴ <https://keras.io>

⁵ <https://www.tensorflow.org/>

3.2.2. Network Fusion

The feature extracting capabilities and characteristics of each single network are different. Therefore, effective fusion algorithms are also introduced to usually improve accuracy. The fusion model takes the output from the multiple single network algorithms and determines the learning accuracy. Our model fusion strategy is shown in Figure 3. All the fused models include a convolutional stage and a full connected stage. At the convolutional stage, the data set is inputted to the respective single network model that has already been trained (see 3.2.1), and undergoes a complete training with frozen parameters. Then, the output features of multiple models are concatenated at the fully connected stage and flattened. Here, we use two new FC layers with 8 and 2 neurons, respectively. For the fused models, we only train and update the parameters of the two new FC layers, whose training procedure is the same as Section 3.2.1. The labels of our fused models are listed in Table 3.

3.3. Visualization Analysis

Feature Visualization: Deep learning algorithms have been widely applied in various scenarios, but their decision-making processes are opaque to humans. Therefore, these models are often perceived as black boxes. It is necessary to quantify and visualize the features that extracted by Neural Networks. Selvaraju et al. (2017) proposed an approach to provide visual explanations for deep learning algorithms labeled as Gradient-weighted Class Activation Mapping (Grad-CAM). Grad-CAM produces a heat-map that highlights the crucial regions of an image by using the gradients of the target features from the final convolutional layer. This means that the feature maps from the final layer are extracted, and each channel in those features is weighted with the gradient of the class with respect to the channel. Referencing to Selvaraju et al. (2017), the heat-map of features, $L_{Grad-CAM}^c$, are computed in this work, and presented in the bottom of each panels in Figure 1 as examples. The most significant feature is the maximum value of the mapping-curves of features obtained by summing the heat-map of features along the channel axis.

Dimensionality Reduction Visualization: The feature map from the final convolutional layer is a high-dimensional and complex dataset, which makes it challenging to distinguish and compare bursts, as it is difficult to determine which information is most important. Reducing high-dimensional data and representing it in 2D or 3D could directly visualize the pattern of data distribution. Maaten & Hinton (2008) proposed a non-linear dimensionality reduction algorithm, T-distributed Stochastic Neighbor Embedding (t-SNE), which has great application value in big data analyzing. Here we apply the t-SNE technique to analyze the feature map of test set, and use the `sklearn.manifold.TSNE` method to implement t-SNE by scikit-learn⁶. As a comparison, the count map of samples in test set without normalized preprocessing are also analyzed. The custom parameter *Perplexity* specifies the importance of local or global structure, which generally represent the number of nearest neighbors of each data. The custom parameter *Init* represents the initialization of embedding. We respectively set the *Perplexity* (ranging in 5, 20, 40, 60 and 80) and *Init* (ranging in *pca* and *random*) to check the classification stability of t-SNE, which refers to the hyper-parameter settings in these publications(Jespersen et al. 2020; Salmon et al. 2022; Steinhardt et al. 2023). By visualizing and analyzing the effect of the distinction between the two category data, we chose *Perplexity* with 20 and *Init* with ‘random’ as the optimal setting, while the other hyper-parameters take the default values of the `sklearn.manifold.TSNE` method.

4. RESULT

4.1. Model Performance

Three data sets are constructed from over ten years observation data of Fermi/GBM as shown in Table 1, and their time bins are 256, 128, and 64 ms, respectively. We build three single network models, *plain*-CNN, ResNet and ResNet-CBAM, and train them on each data sets. The learning curves for model training are displayed in Figure 4 which reveals partial overfitting of our models. We prevent the overfitting issue by truncating model training procedure through the use of early stopping mechanisms. Those models are evaluated using test sets with different time bins, and their performances are illustrated by four metrics, *Accuracy*, *Precision*, *Recall* and *F1-score* respectively, see Appendix A. The performance metrics of each model in the training set, validation set, and test set are displayed in Table 2. The specific recognition rate of the models for the samples of each category could be represented by the confusion matrix. Figure 5 shows the performance of each model on the confusion matrix. With incorporation of the residual module and attention mechanism, it strengthens the generalization ability of our CNN models. It can be quite clearly grasped

⁶ <https://scikit-learn.org/>

to discriminate what an optimal model the ResNet-CBAM trained on the 64 ms data set is. The Receiver Operating Characteristics (ROC) is another useful way to compare models from an immediate perspective. The area under the ROC curve indicates the ability of classification accuracy. The ROC curves of our single network models are shown in Figure 6. The ResNet-CBAM trained on 64 ms data set obtains the largest area among those ROC curves, which also indicates its powerful classification ability.

The fused models and their performance are shown in Table 3. The overall performance of all fused models exceed 94%, and is better than single network models. However, the improvement is relatively limited. The *plain*-CNN+ResNet+ResNet-CBAM model trained with the 64 ms data set performs well among those fused models. Whereas, during training and testing, we find fused models consume more resources and exhibit low efficiency.

The Grad-CAM method is selected to perform visualization analysis on features that produced by the optimal model. This method is effective in locating objects in images based on category conditions. The results, namely heat-maps, are shown as the bottom of each panels in Figure 1. Here, we only show four GRBs events corresponding to different morphologies. The most interesting areas of the model, namely the most prominent area in heat-map, are mainly located at the burst period. In addition, the t-SNE technique is applied to reduce the dimensionality of count maps in test set, with the 2D and 3D result presented in Figure 7. The behavior of the GRB category and the non-GRB category are indistinguishable. For GRB category, there are no obvious boundary with various duration. Furthermore, feature maps produced by the optimal model, are also applying t-SNE method. Figure 11 and Figure 11 depict the results of dimensionality reduction, where the two categories of the test set are distinguished in two separate areas, and there is also no clear distribution of duration among the categories.

4.2. Application Result

We applied the optimal model to search GRBs with a whole year data that observed by NaI detectors onboard Fermi/GBM from July 1, 2021 to June 30, 2022. A sliding time window was designed to extract data from each daily TTE of NaI detectors continuously, with its length of 120 seconds and with a step size of 110 seconds. We extract data in reverse when the end of the data file is less than 120 seconds. It is important to note here that the time windows for each detector are isochronous for the convenience of subsequent joint analysis. Another important point to note that we selected *sliding* windows within the range of Good Time Interval (GTI) to ensure each time window is completely contained in the GTI. The data were processed into count maps, which is consistent with Section 2. Finally, 3.05 million count maps with bin size of 64 ms were obtained. These count maps are inputted into the optimal model, and the classification of GRB or non-GRB is determined. There are 39,515 classified GRBs that identified as initial events, a further screening of those events is needed for searching candidates of GRB, and the corresponding heat-maps and mapping-curves of feature were outputted previously.

The screening process consists of two steps: 1) time filtering: if there are fewer than two initial events in the same time window, then these events are excluded. The purpose of this step is to ensure that each candidate is detected by at least two detectors. 2) location filtering: in each time window, we record the burst moment of the most significant feature in mapping-curves of every initial event. We sort these moments of bursts and search sequentially for a 20 seconds region from the first moment of burst. If there are at least two burst within a 20 seconds interval, then they are considered together as a candidate, otherwise repeat this searching process with the remaining initial events. In other words, there might exist more than one candidate in each time window, and it is important to retain as much information about the bursts as possible. The South Atlantic Anomaly (SAA) is a geomagnetic anomaly region that covers the eastern of South America and the south atlantic ocean. Fermi/GBM turns off its detectors when crossing over the SAA region to protecti detectors. Therefore, data in this period should be excluded. We considered this situation and GTI in the data pre-processing process. However, many events are still located in the SAA region, so we exclude 45 events. After the aforementioned screening process, a total of 1963 candidates were obtained.

We matched these candidates with the catalog of Fermi/GBM triggers⁷, sub-threshold triggers⁸ and sub-threshold GRBs. The information of optimum matching is only about bursting time. The result is shown in Table 4. Approximately 98% public GRBs of GBM instrument are matched with our candidates. The mapping-curves of features of the 8 missing GRBs are shown in Figure 12. We performed a checkback with our initial events, and find three of them are identified as single initial events within 120 s time window. They seem like single detector triggered events. For the

⁷ <https://heasarc.gsfc.nasa.gov/W3Browse/fermi/fermigtrig.html>

⁸ https://gcn.gsfc.nasa.gov/gcn_fermi_gbm_subthresh_archive.html

other 4 missed GRBs, we found that they are classified as non-GRB category with causes unknown. For the missed GRB 211031175, there are two corresponded initial events, but the time interval of the most significant features is longer than 20 seconds. Moreover, the significance of most missed GRBs are barely about $5\sim 6\sigma$, which may also be the reason for missing. There are still a large number of candidates that correspond to other triggering types, e.g., solar flare (SFLARE), soft gamma-ray repeater (SGR), local particles (LOCLPAR), etc. Morphologically speaking, those type triggers look like GRB events from their features of light curves and spectrum considerably. In general, the spatial locations of those triggers are apparently different from those of GRBs. For our binary classification method, the training process and data sets do not include the location information of bursts. Therefore, we lack a way to screen candidates based on location information.

In addition, we further compared our candidates with published sub-threshold GRBs and sub-threshold triggers of Fermi/GBM. There were 11 sub-threshold GRBs published on the Gamma-ray Coordinates Network (GCN) circular⁹ totally in this year. Eight sub-threshold GRBs therein were found to be temporally coherent with our candidate. Our model classified them as GRB category with high confidence, whose mapping-curves are displayed in Figure 13. Their characteristics performed by our model are prominent and accord with analysis in GCN. One sub-threshold GRB (with GCN number 30421) is individually comparable to an initial event that shows high confidence in one detector only. The remaining two GRBs were not successfully identified by our model. The result demonstrates that our model exhibits excellent discriminative ability for low-threshold gamma-ray burst signals. Furthermore, we conducted a comparative analysis between our candidates and the sub-threshold triggers that may potentially include weak GRBs. With the screening conditions we set, 64 sub-threshold triggers therein were effectively distinguished. The search accuracy rate is a bit low, about 9.96%. Our manual inspection reveal 120 initial events that still have extremely high confidence level. This suggests that by loosening the screening conditions, these events might be treated as GRB category. The identification accuracy would increase to 28.66%.

By comparing GRBs in Fermi burst catalog with GRBweb¹⁰, we find additional 51 GRBs are not listed in Fermi burst catalog but were detected by other instruments. Among them, there are 17 GRBs without corresponding GBM continuous data. Fermi/GBM has observed the other 34 GRBs normally during their burst phase. In other words, GBM burst advocates (BA) did not ascertain these GRBs via ground analysis. Amazingly, 21 of the 34 GRBs are temporally matched with our unknown events discovered by our model. Among them, 5 GRBs show significant signals in multiple detectors, 16 GRBs only display in single detector, and the other 13 GRBs do not have burst signal in the corresponding count maps. The GRB names, relevant GCN numbers, instruments and the analysis results of our discovered GRBs are listed in Table 5. Interestingly, we find the trigger time of two GRBs, GRB220308A and GRB220403C (from GRBweb), are close together with GRB220308233 and GRB220403424 that listed in the Fermi/GBM catalog, respectively. In our opinion, these two GRBs could be peculiar long bursts with precursor component comprised long interval comparable with GRB160625B (Zhang et al. 2018a) and GRB221009A (An et al. 2023).

The Figure 15 illustrates our process of searching for candidates and the results that compared with known events. For verifying the scientific significance of these 1558 unknown events, we could compare them with other published intense bursts in this year, e.g., magnetars, solar flares. Here we only choose well known magnetar SGR J1935+2154 as a target. By using the sub-threshold search algorithm, Lin et al. (2020a), Lin et al. (2020b), Zou et al. (2021), Ibrahim et al. (2023) and Xie et al. (2022) have found over 200 new bursts from SGR J1935+2154 than Fermi trigger catalog. And it is important to note that there are 74 duplicate bursts in these references after our verification. Then, we compared these new bursts with our unknown events. 24 of the 1558 unknown events corresponded to these newly discovered bursts. The contrasted results are shown in Table 6, and their nameplate (ID), relevant researches, and our analysis results are listed in Table 7. This indicates that our model has the capability to identify weak bursts comparable to manual analysis. It means our unknown events could potentially comprise some non-negligible scientific events. Besides, the other 1529 unknown events are respectively shown in Table 8 ($\text{SNR} \geq 5\sigma$), Table 9 ($\text{SNR} < 5\sigma$) and Table 10 (without SNR) according to their SNR information. The T_{90} and SNR are calculated with reference to Appendix B.

The information of duration and location are necessary to analysis our searched candidates. However, our examination demonstrate that most of the candidates are too weak for such calculation. The prominent areas in heat-maps are

⁹ https://gcn.gsfc.nasa.gov/gcn3_archive_GRB.html

¹⁰ https://user-web.icecube.wisc.edu/~grbweb_public/Summary_table.html

relevantly corresponded with the burst region of GRBs, hence we can use the period of prominent area to characterize the duration of the candidate. Employing the mapping-curves of feature (see Figure 14b) for each candidate and normalizing the summed value of feature per bin, the corresponding feature curves are finally formed, see Figure 14a. The duration of each initial event T_F is determined as the time period of the prominent area exceeds the threshold. By verifying of the duration T_{90} and T_F of some GRB samples, we establish a correlation between Intersection over Union (IoU, always ≤ 1) ratio, as shown in Figure 14c. The threshold is empirically selected as 0.2 and T_F of initial events for each candidate is summed as its duration $T_{90,F}$, shown as the green area of Figure 14b. We use $T_{90,F}$ to characterize the duration of bursts/candidates. The heat-map of this example is marked as $T_{90,F}$, see Figure 14d, which distinctly demonstrates the close connection between prominent area and $T_{90,F}$.

The $T_{90,F}$ of all 1529 unknown candidates are computed and their start times are shown in Table 8, Table 9 and Table 10, respectively. Based on the start time of each unknown candidate, we obtained its corresponding locations of Fermi satellite in orbit, shown in Figure 16. The candidates with different SNR are displayed. Some candidates show significant signals only in a single bin, thus we label them as spark like events. Our spark like events, sub-threshold GRBs, and other 5 known GRBs are also marked. Considering the correlation between certain signal, e.g., particle events (LOCLPAR), TGF (Terrestrial Gamma-ray Flashes), with geomagnetic latitude (McIlwain L), we also present McIlwain L in the figure. We find there is no obvious distribution or relationship between our candidates and McIlwain L. The localization results of the candidates in these tables are calculated based on the algorithm in the Appendix C. The localization of these 181 unknown events, with their T_{90} valid computing, were calculated and shown in Figure 17. The localization error of these candidates are tightly related to their significance. The candidates with $\text{SNR} \geq 5\sigma$ including spark like events present accurate localization. From these unknown candidates, there are 4 events located in the approaching region of SGR J1935+2154, and their light curves show simple peak shape that similar to burst of SGR. We also sign 24 candidates corresponded to SGR J1935+2154 mentioned above. We suggest those 4 events are probable candidates of SGR J1935+2154. There are 41 unknown candidates located in earth occlusion region, and 15 candidates would direct to sun through their localization. Referring localization information, the angular distribution of these localized candidates is fairly uniform, which reveal the potential cosmic signals they are.

5. DISCUSSION AND CONCLUSION

As the research hotspots of multi-messenger and time-domain astronomy in particular, under the limitations of the existing data sets, it is a hot pursuit for researchers to making rational use of GRBs light curves and spectra to realize rapid and accurate discovery of their pertinent and meaningful information. Therefore, deep learning methods have been gradually applied and have achieved great success in terms of identifying, classifying, and forecasting burst events and phenomena of astronomy. In this paper, the supervised deep learning methods were applied to identify GRBs from the Fermi/GBM TTE data. Referring to the burst catalog of GBM, we categorized GRBs and non-GRBs sets and achieved the aim of training valid models. Then we applied the optimal model to identify GRB candidates from the approaching one-year TTE data.

Thousands of count maps of GRBs and non-GRBs were used, and the valid training set, validation set, and test set were built, see Table 1 for detail. The selected 2560 GRBs were multiplied by the number of triggered detectors, and they were taken as the samples of GRB category. These samples were distributed into data sets in three time period. Correspondingly, daily data products after filtering out the burst TTE data were randomly selected as samples of non-GRB category. Our sample construction method is conducive to minimizing the limitation of insufficient positive sample size as much as possible. Moreover, the reasonable ratio of each dataset is advantageous to ensure the balance of data distribution. Furthermore, the time period distributing of samples would avoid data confusion. There are three types datasets that contain samples with bin size of 256, 128, and 64 ms, respectively, and the purpose is to consider the effect of time resolution. A total energy of 128 channels were chosen for all samples. Therefore, the pixel matrix of count maps of samples is 128*1875, 128*938 and 128*469.

There are three single network models structured in our work, named as *plain*-CNN, ResNet and ResNet-CBAM, respectively, shown in Figure 2. Base on the general Conv-block, we progressively added residual modules, residual-attention modules to the *plain*-CNN model, and appeared to be working well. The three models are trained on three data sets with different time bins separately. We find that the ResNet-CBAM model achieved the highest accuracy on the 64 ms data set. This model incorporates the attention mechanism of spatial and channel dimensions, as proposed by Woo et al. (2018), to significantly enhance the feature extraction ability, which is crucial for improving classification. The training curves of models in Figure 4 show tendency of overfitting, even though we employed the data expansion,

dropout and early stopping mechanisms. Subsequently, collection of burst events, data augmentation, and model hyper-parameter optimization may solve this problem. Relatively, as shown clearly in Table 2 and Figure 5, models with same architecture that trained on data sets of smaller time bin shown better performance. The models achieve high accuracy in the training set, validation set and test set. The model's comparable accuracy on the validation and test sets indicates its strong generalization capability. Intuitively the ROC curves in Figure 6 have indicated the powerful classification ability of ResNet-CBAM model. It is possible that count map with shorter time bins contains more fine-grained information of bursts, as it is generally agreed that the variation of some burst structure behave differently within different time bin (Bhat 2013). Different model architectures exhibit varied performance as due to their feature extracting capability. We tried to fuse those single network models through four combinations. Overall of fusion architecture is shown in Figure 3. Four fusion algorithms with new FC layers are structured and trained with three different bin size data sets with their performance shown in Table 3. Fusion models improve accuracy indeed, however, they consume more computing resources and the improvement is not impressive yet.

In order to better understand the deep learning models, visualization analysis methods are employed. We use Grad-CAM approach to produce heat-map of features that extract by deep learning models. The bottom panels in Figure 1 show the examples of the results which were extracted by the final convolutional layer of optimal model viz the ResNet-CBAM that trained on 64 ms bin data set. From the mapping-curves of features we achieved, we could clearly find the magnitude of the bursts in these two feature figures. The t-SNE technique is also used for visualizing analysis. For comparison, the count maps and feature maps in test set, corresponding to unapplied and applied deep learning methods, are visualized as 2D and 3D diagrams, respectively shown in Figure 7. The feature maps are output from the last convolutional layer of optimal model. Both 2D and 3D diagrams visualized from the initial count maps in test set are difficult to distinguish between GRBs and non-GRBs. By contrast, the 2D and 3D diagrams obtained from feature maps shown distinct distribution and boundaries between GRBs and non-GRBs. This directly demonstrates the effectiveness of our deep learning method in classifying bursts. For reckoning the hidden physical basis of classification, we embedded information of the SNR, duration, hardness ratio, and hardness ratio deviation of these GRBs into diagrams, shown in Figure 8, Figure 9, Figure 10, and Figure 11. We find such a black box that extracted features and classified decision are involved in these physical information. Supervised deep learning algorithms, with the input of the observed identification samples, can classify different categories into distinct clusters. The clusters show high correspondence with of GRBs and non-GRBs in high accuracy. Visualizing analysis of count maps and feature maps by utilizing the t-SNE technique, a significant difference between the results of two classifications is observed. By inputting feature maps produced by ResNet-CBAM model, GRBs and non-GRBs are adequate clustered into different regions, which suggests the feature extraction of our trained optimal model is powerful and effective. For the input of GRBs that identified by Fermi, it is possible that some GRB samples may have been incorrectly classified as non-GRBs (FN samples). By analyzing the classification results of the test set via the optimal model, we found that about 6% samples of the GRB category were indeed misclassified. These embedded physical information could help us to understand the critical features of the identifying process of our optimal model. We find most of these FN samples were short in duration, low in significance, and abnormal in hardness deviation, which suggests that these observed traits have high weight ratio for decision making of classification judgment. This suggests that these observed characters have a high weight ratio for decision making of classification judgment.

The optimal model is applied on one year observation data of Fermi/GBM, with 1963 candidates identified (see Figure 15 and Table 4). By comparing them with the trigger catalog of Fermi, we find most of the published GRBs were distinguished. A number of other types of triggers are also retrieved, showing that triggers are very complex and highly similar to GRB type within the existing data dimensions (count maps data). Therefore non-GRB type triggers may have been identified by our algorithm of binary classification. It suggests that upgrade of the data dimension in the future is necessary, such as adding of location information from multi-detectors observations, time-resolved spectral information, light curves in different energy channel, etc. None of the TGF events match unknown candidates, which probably due to their extremely short duration (typically 0.1 ms (Von Kienlin et al. 2020)) and their morphologies are completely different from GRBs. More than six hundred weak trigger signals, sub-threshold triggers, are not explicitly categorized by Fermi, they are too weak to distinguish, and rarely associate with our candidates. Currently, our positive samples of training sets are no other than GRBs in Fermi burst catalog. It is a disadvantage factor for identifying sub-threshold triggers. Suppose with the addition of such manual sub-threshold triggers to the training set, the trained model could provide stronger capability to extract features of weak triggers which would be the bursts from distant universe. Admittedly sub-threshold GRBs are too intrinsically weak or viewed with unfavorable instrument

geometry to initiate an onboard trigger of Fermi/GBM (Kocevski et al. 2018). Undeniably, it is worth identifying sub-threshold GRBs with a lot of efforts, of which are suggested as the counterparts of gravitational waves, fast radio bursts or other transient events (Goldstein et al. 2019; Yang et al. 2020; Tohuvavohu et al. 2020). The deep learning method could effectively uncover hidden and weak signals. In our candidates, most public sub-threshold GRBs of Fermi/GBM are precisely identified. Sufficient samples of sub-threshold GRBs would help us to train a more accurate algorithm with high efficiency than manual work (Zhang et al. 2018b; Yang et al. 2021). In addition, the no matching candidates, totally are the 1558 unknown events, are potentially have the value of scientific research. There are a number of additional bursts are discovered from SGR J1935+2154 beyond the Fermi/GBM trigger catalog by using the sub-threshold search algorithm, see Figure 6. There are 24 candidates from our optimal model are corresponding to these bursts. Through the SNR and localization analysis for the unknown candidates, we notice that 3 events apparently came from the SGR J1935+2154, and the spatial distribution of these localized candidates are uniform. These offer unambiguous clue that our candidates would correlate with potential violent outbursts from astronomy objects. Subsequently deeper analysis would provide more associations between our candidates and other known bursts subsequently.

The CNN provide higher sensitivity in many scenarios, but lack interpretability in prediction. The visual analysis reveals that our model accurately identifies the burst characteristics of GRBs, which indicates that the model is accurate and effective. Compared to traditional trigger search algorithms implemented by peak detection, our approach makes more reasonable representation of the characteristics of GRBs. There are many types of burst phenomena besides GRB, such as fast radio bursts, soft gamma repeaters. Using multiple types of burst data in dataset to train the deep learning model, the visual analysis method enables a precise comparison and analysis of the characteristics and physical patterns of different bursts. The average elapsed time for the optimal model to classify each count map on GPU (NVIDIA GTX-1080Ti) is 8ms, which means that the model is able to identify GRBs in real time. In the future, our method allows to automate the quick look of scientific achievements with high precision, which is beneficial in guiding rapid follow-up observations. Our method could be adopted as a crucial procedure for the burst advocates (BA) to discover burst events, which assists researchers to improve the detection efficiency of GRBs or other burst events in further analysis. Transfer learning is a advance machine learning method that implements an existing model to a relevant task but only require tiny data set (Yosinski et al. 2014). Gravitational wave high-energy Electromagnetic Counterpart All-sky Monitor (GECAM) satellites (i.e. GECAM-B and GECAM-C) were dedicated to monitoring Gamma-ray transients including GRBs and Soft Gamma Repeaters from the universe with considerable detection capability. With an orbital period of three years in orbit, the GECAM series have detected about two hundreds GRBs¹¹, which were difficult to train large deep learning model for research. Our deep learning models have great potential to be transferred into the data analysis pipelines of the GECAM telescope for distinguishing GRBs accurately. As more observations are available, more data will be collected to training our models continuously, which will be beneficial to effectively enhancing the generalization ability of models. Moreover, the feasibility of embedding tiny deep learning model into Satellite On-Board Computer (OBC) of Gamma-ray monitor telescope for onboard trigger distinguish is also worth exploring further. Take extremely early electromagnetic emission of GRBs as an example, e.g., the prompt optical emissions, the early optical flashes and the X-ray/ultraviolet flares, which are important probes for studying the physical origins and processes of GRBs (Piran et al. 1999; Zhang et al. 2003; Racusin et al. 2008; Xin et al. 2023; Jin et al. 2023). These emissions are extremely brief and of high intensity, making challenges for observation and study. Real-time and accurate identification of trigger signals by deep learning models, and rapid transmission of information through satellite communication networks such as BAS of GECAM (Huang et al. 2023) are crucial for follow-up observations by other telescopes in multi-wavelength bands. It enables researchers to capture multi-wavelength electromagnetic emissions as early as possible.

6. ACKNOWLEDGEMENTS

We would like to thank Dr. Xiang Ma, Dr. Riccardo Crupi, Dr. Shi-Jie Zheng, Dr. Zheng-De Zhang, and Dr. Shuo Xiao et al. for helpful discussion. This study is supported by the National Natural Science Foundation of China (Grant Nos. 12103055, U1938201, 12273042, 12133007, U1938108, 41827807, and 61271351), and by the National Key R&D Program of China (2021YFA0718500). This work is also partially supported by the Strategic Priority Research Program of the CAS under grant No. XDA15360300. Z.-C. Z. is supported by the National Natural Science

¹¹ <https://gcn.gsfc.nasa.gov/gcn/gecam.events.html>

Foundation of China (Grant No. 12233002). Bing li acknowledges support from the National Astronomical Science Data Center Young Data Scientist Program (grant No. NADC2023YDS-04).

7. DATA AVAILABILITY

The code, data sets, and candidate list are available upon reasonable request.

REFERENCES

- Abraham, S., Mukund, N., Vibhute, A., et al. 2019, A machine learning approach for GRB detection in AstroSat CZTI data. <https://arxiv.org/abs/1906.09670>
- Agarwal, D., Aggarwal, K., Burke-Spoliar, S., Lorimer, D. R., & Garver-Daniels, N. 2020, MNRAS, 497, 1661, doi: [10.1093/mnras/staa1856](https://doi.org/10.1093/mnras/staa1856)
- An, Z.-H., Antier, S., Bi, X.-Z., et al. 2023, arXiv preprint arXiv:2303.01203
- Atteia, J. L., Heussaff, V., Dezelay, J. P., et al. 2017, ApJ, 837, 119, doi: [10.3847/1538-4357/aa5ffa](https://doi.org/10.3847/1538-4357/aa5ffa)
- Band, D., Matteson, J., Ford, L., et al. 1993, ApJ, 413, 281, doi: [10.1086/172995](https://doi.org/10.1086/172995)
- Band, D. L. 2002, The Astrophysical Journal, 578, 806
- Baron, D. 2019, arXiv preprint arXiv:1904.07248
- Bhat, N. P. 2013, EAS Publications Series, 61, 45
- Blackburn, L., Briggs, M. S., Camp, J., et al. 2013, arXiv preprint arXiv:1303.2174
- Crupi, R., Dilillo, G., Bissaldi, E., et al. 2023, Experimental Astronomy, 56, 421
- De, S., Maitra, W., Rentala, V., & Thalapillil, A. M. 2022, arXiv preprint arXiv:2206.05296
- de Andres, D., Cui, W., Ruppin, F., et al. 2022, Nature Astronomy, 6, 1325
- Glorot, X., Bordes, A., & Bengio, Y. 2011, in Proceedings of the fourteenth international conference on artificial intelligence and statistics, 315–323
- Goldstein, A., Hamburg, R., Wood, J., et al. 2019, arXiv e-prints, arXiv:1903.12597. <https://arxiv.org/abs/1903.12597>
- Goode, S., Cooke, J., Zhang, J., et al. 2022, Monthly Notices of the Royal Astronomical Society, 513, 1742
- Gruber, D., Goldstein, A., Weller von Ahlefeld, V., et al. 2014, ApJS, 211, 12, doi: [10.1088/0067-0049/211/1/12](https://doi.org/10.1088/0067-0049/211/1/12)
- He, K., Zhang, X., Ren, S., & Sun, J. 2015, in Proceedings of the IEEE international conference on computer vision, 1026–1034
- He, K., Zhang, X., Ren, S., & Sun, J. 2016, in 2016 IEEE Conference on Computer Vision and Pattern Recognition (CVPR), 770–778, doi: [10.1109/CVPR.2016.90](https://doi.org/10.1109/CVPR.2016.90)
- Hezaveh, Y. D., Levasseur, L. P., & Marshall, P. J. 2017, Nature, 548, 555
- Huang, Y., Shi, D., Zhang, X., et al. 2023, arXiv preprint arXiv:2307.04999
- Ibrahim, A. I., et al. 2023, The Astrophysical Journal, 950, 121
- Jespersen, C. K., Severin, J. B., Steinhardt, C. L., et al. 2020, The Astrophysical Journal Letters, 896, L20
- Jia, P., Liu, W., Liu, Y., & Pan, H. 2023, The Astrophysical Journal Supplement Series, 264, 43
- Jin, Z.-P., Zhou, H., Wang, Y., et al. 2023, arXiv preprint arXiv:2301.02407
- Kembhavi, A., & Pattnaik, R. 2022, Journal of Astrophysics and Astronomy, 43, 76
- Kingma, D. P., & Ba, J. 2017, Adam: A Method for Stochastic Optimization. <https://arxiv.org/abs/1412.6980>
- Kocevski, D., Burns, E., Goldstein, A., et al. 2018, The Astrophysical Journal, 862, 152
- Kouveliotou, C., Meegan, C. A., Fishman, G. J., et al. 1993, ApJL, 413, L101, doi: [10.1086/186969](https://doi.org/10.1086/186969)
- Kumar, P., & Zhang, B. 2015, PhR, 561, 1, doi: [10.1016/j.physrep.2014.09.008](https://doi.org/10.1016/j.physrep.2014.09.008)
- Kumari, A., et al. 2023, arXiv preprint arXiv:2305.09596
- Lecun, Y., Bengio, Y., & Hinton, G. 2015, Nature, 521, 436, doi: [10.1038/nature14539](https://doi.org/10.1038/nature14539)
- Lin, L., Göğüş, E., Roberts, O. J., et al. 2020a, The Astrophysical Journal Letters, 902, L43
- . 2020b, The Astrophysical Journal, 893, 156
- Maaten, L. v. d., & Hinton, G. 2008, Journal of machine learning research, 9, 2579
- Merz, G., Liu, Y., Burke, C. J., et al. 2023, Monthly Notices of the Royal Astronomical Society, 526, 1122
- Mészáros, P. 2019, Mem. Soc. Astron. Italiana, 90, 57. <https://arxiv.org/abs/1904.10488>
- Minaev, P. Y., & Pozanenko, A. S. 2020, MNRAS, 492, 1919, doi: [10.1093/mnras/stz3611](https://doi.org/10.1093/mnras/stz3611)
- Narayana Bhat, P., Meegan, C. A., von Kienlin, A., et al. 2016, ApJS, 223, 28, doi: [10.3847/0067-0049/223/2/28](https://doi.org/10.3847/0067-0049/223/2/28)
- Nevavuori, P., Narra, N., & Lipping, T. 2019, Computers and electronics in agriculture, 163, 104859
- Ohmori, N., Yamaoka, K., Yamauchi, M., et al. 2019, PASJ, 71, 76, doi: [10.1093/pasj/psz054](https://doi.org/10.1093/pasj/psz054)

- Parmiggiani, N., Bulgarelli, A., Fioretti, V., et al. 2021, *The Astrophysical Journal*, 914, 67
- Parmiggiani, N., Bulgarelli, A., Ursi, A., et al. 2023, *The Astrophysical Journal*, 945, 106
- Pinchuk, P., & Margot, J.-L. 2022, *The Astronomical Journal*, 163, 76
- Piran, T., et al. 1999, *The Astrophysical Journal*, 520, 641
- Preece, R., Goldstein, A., Bhat, N., et al. 2016, *ApJ*, 821, 12, doi: [10.3847/0004-637X/821/1/12](https://doi.org/10.3847/0004-637X/821/1/12)
- Qiu, R., Krastev, P. G., Gill, K., & Berger, E. 2023a, *Physics Letters B*, 840, 137850
- . 2023b, *Physics Letters B*, 840, 137850
- Racusin, J. L., Karlov, S., Sokolowski, M., et al. 2008, *Nature*, 455, 183
- Salmon, L., Hanlon, L., & Martin-Carrillo, A. 2022, *Galaxies*, 10, 78
- Selvaraju, R. R., Cogswell, M., Das, A., et al. 2017, in *Proceedings of the IEEE international conference on computer vision*, 618–626
- Sen, S., Agarwal, S., Chakraborty, P., & Singh, K. P. 2022, *Experimental Astronomy*, 53, 1
- Shi, J.-H., Qiu, B., Luo, A.-L., et al. 2023, *Monthly Notices of the Royal Astronomical Society*, 520, 2269
- Srivastava, N., Hinton, G., Krizhevsky, A., Sutskever, I., & Salakhutdinov, R. 2014, *J. Mach. Learn. Res.*, 15, 1929–1958
- Steinhardt, C. L., Mann, W. J., Rusakov, V., & Jespersen, C. K. 2023, arXiv preprint arXiv:2301.00820
- Stopka, F., Bhattacharyya, S., de Austri, R. R., et al. 2023, *Astronomy & Astrophysics*, 680, A109
- Tohuvavohu, A., Kennea, J. A., DeLaunay, J., et al. 2020, *The Astrophysical Journal*, 900, 35
- Ulas, B. 2023, arXiv preprint arXiv:2306.02686
- Ulyanov, D., Vedaldi, A., & Lempitsky, V. 2016, arXiv e-prints, arXiv:1607.08022.
<https://arxiv.org/abs/1607.08022>
- Venn, K., Fabbro, S., Liu, A., et al. 2019, arXiv preprint arXiv:1910.00774
- Von Kienlin, A., Meegan, C., Paciesas, W., et al. 2020, *The Astrophysical Journal*, 893, 46
- Wang, F., Zou, Y.-C., Liu, F., et al. 2020, *ApJ*, 893, 77, doi: [10.3847/1538-4357/ab0a86](https://doi.org/10.3847/1538-4357/ab0a86)
- Woo, S., Park, J., Lee, J.-Y., & Kweon, I. S. 2018, in *Proceedings of the European conference on computer vision (ECCV)*, 3–19
- Wu, Y., Tao, Y., Fan, D., Cui, C., & Zhang, Y. 2024, *Monthly Notices of the Royal Astronomical Society*, 527, 1163
- Xie, S.-L., Cai, C., Xiong, S.-L., et al. 2022, *Monthly Notices of the Royal Astronomical Society*, 517, 3854
- Xin, L., Han, X., Li, H., et al. 2023, *Nature Astronomy*, 1
- Yang, X., Zhang, S., Wang, J., et al. 2021, *Monthly Notices of the Royal Astronomical Society*, 507, 3238
- Yang, Y.-S., Zhong, S.-Q., Zhang, B.-B., et al. 2020, *ApJ*, 899, 60, doi: [10.3847/1538-4357/ab9ff5](https://doi.org/10.3847/1538-4357/ab9ff5)
- Yosinski, J., Clune, J., Bengio, Y., & Lipson, H. 2014, *Advances in neural information processing systems*, 27
- Zhang, B., Kobayashi, S., & Mészáros, P. 2003, *The Astrophysical Journal*, 595, 950
- Zhang, B.-B., Zhang, B., Castro-Tirado, A. J., et al. 2018a, *Nature Astronomy*, 2, 69
- Zhang, Y. G., Gajjar, V., Foster, G., et al. 2018b, *The Astrophysical Journal*, 866, 149
- Zhao, Y., Xue, W.-C., Xiong, S.-L., et al. 2023, *The Astrophysical Journal Supplement Series*, 265, 17
- Zhao, Y., Xue, W., Xiong, S., et al. 2023a, arXiv e-prints, arXiv:2209.13088. <https://arxiv.org/abs/2209.13088>
- Zheng, Y., Li, X., Yan, S., et al. 2023, *Monthly Notices of the Royal Astronomical Society*, 521, 5384
- Zou, J.-H., Zhang, B.-B., Zhang, G.-Q., et al. 2021, *The Astrophysical Journal Letters*, 923, L30

APPENDIX

A. MODEL EVALUATION METRICS

Generally, the performance of a deep learning model for classification is described by four metrics, namely, *Accuracy*, *Precision*, *Recall*, and *F1-score*, as follows

$$\text{Accuracy} = \frac{TP + TN}{TP + TN + FP + FN} \quad (\text{A1})$$

$$\text{Precision} = \frac{TP}{TP + FP} \quad (\text{A2})$$

$$\text{Recall} = \frac{TP}{TP + FN} \quad (\text{A3})$$

$$\text{F1-score} = \frac{2 \times \text{Precision} \times \text{Recall}}{\text{Precision} + \text{Recall}} \quad (\text{A4})$$

where TP , TN , FP and FN represent the number of true positives, true negatives, false positives and false negatives respectively.

B. CALCULATION OF T_{90} AND SNR

We first fit the background using a polynomial function with order 1 for the summed light curve of triggered detectors. The background region is chosen from ($T_{\text{begin}} - 15$ s to $T_{\text{begin}} - 5$ s) and ($T_{\text{end}} + 5$ s to $T_{\text{end}} + 15$ s) which is relative to the burst period. The cumulative counts of each bin are plotted by using the background-subtracted light curve. The T_{90} is calculated as $T_{90} = T_{95} - T_5$, where T_{95} and T_5 are the times when 95 percent and 5 percent of the total counts of burst are obtained, respectively. Generally, we choose the range of T_{90} as the source region of burst. We determine the SNR of the source region excess over background fluctuation, by using the following equations:

$$N_{bkg} = N'_{bkg} \times \frac{T_{src}}{T_{bkg}} \quad (\text{B5})$$

where N'_{bkg} and T_{bkg} are the total counts and duration of the background region, respectively. T_{src} is the duration of the source region. Then the SNR can be estimated as:

$$\text{SNR} = \frac{N_{net}}{\sigma_{N_{bkg}}} = \frac{N_{src} - N_{bkg}}{\sqrt{N_{bkg}}} \quad (\text{B6})$$

where N_{src} is the total counts in the source region.

C. LOCALIZATION ALGORITHM OF CANDIDATES

Based on the counts distribution of detectors in different directions, a Bayesian localization method is proposed to localize bursts using the Poisson data with Gaussian background (PGSTAT) profile likelihood (Zhao et al. 2023a; Zhao et al. 2023). Due to the high-energy transients localization capability of this algorithm, we apply it to locate our candidates. The T_{90} is used as the source interval of the candidates. We utilize the GBM Data Tools¹² to implement the polynomial fitting to the background. The estimated background of the source interval could be obtained by interpolation. Spectral data from the source interval of the 12 NaI detectors are used to perform fixed template localization. We adopt three fixed spectral templates (see also the spectral templates of Table 4 in Zhao et al. (2023)) through the Bayesian localization method with PGSTAT profile likelihood. The maxima of the maximum PGSTAT profile likelihood is taken as the location result.

¹² GBM Data Tools: https://fermi.gsfc.nasa.gov/ssc/data/analysis/rmfit/gbm_data_tools/gdt-docs/.

Table 1. Description of data set.

Partition	Nu. of GRB	Nu. of non-GRB	Data Period Definition (UTC)
Training set	3082	6000	Jul 14, 2008 - Dec 31, 2014
Validation set	1507	2000	Jan 1, 2015 - Dec 31, 2017
Test set	1741	2000	Jan 1, 2018 - Jun 31, 2021

Table 2. The performance of the individual models on the training set, validation set and test set respectively.

Time Scale	Model	Dataset	Accuracy (%)	Precision (%)	Recall (%)	F1-score (%)
256 ms	plain-CNN	Training set	99.37	99.90	98.24	99.06
		Validation set	95.12	97.44	91.04	94.13
		Test set	94.01	97.25	89.66	93.30
	ResNet	Training set	98.95	99.93	96.98	98.43
		Validation set	95.49	98.07	91.30	94.57
		Test set	94.84	98.19	90.58	94.23
	ResNet-CBAM	Training set	98.65	99.59	96.43	97.98
		Validation set	95.83	97.88	92.30	95.01
		Test set	95.08	98.08	91.21	94.52
128 ms	plain-CNN	Training set	99.44	99.96	98.41	99.18
		Validation set	95.83	98.22	91.97	94.99
		Test set	95.26	98.99	90.75	94.69
	ResNet	Training set	98.00	99.25	94.84	96.99
		Validation set	96.17	98.51	92.50	95.41
		Test set	95.29	98.69	91.09	94.74
	ResNet-CBAM	Training set	98.73	99.83	96.43	98.10
		Validation set	96.49	98.59	93.16	95.80
		Test set	95.99	99.13	92.18	95.53
64 ms	plain-CNN	Training set	99.18	99.60	97.98	98.78
		Validation set	96.49	98.39	93.36	95.81
		Test set	96.15	98.30	93.33	95.75
	ResNet	Training set	99.21	99.53	98.15	98.84
		Validation set	96.60	97.40	94.62	95.99
		Test set	96.20	97.96	93.79	95.83
	ResNet-CBAM	Training set	99.22	99.70	98.02	98.85
		Validation set	96.94	98.20	94.62	96.30
		Test set	96.57	98.61	93.96	96.23

NOTE—Bold text indicates the metrics for which the model performed best on the test set.

Table 3. Summary of four metrics describing the performance of fused models.

Time Scale	Model	Accuracy (%)	Precision (%)	Recall (%)	<i>F1-score</i> (%)
256 ms	<i>plain</i> -CNN+ResNet	94.86	98.61	90.23	94.24
	<i>plain</i> -CNN+ResNet-CBAM	94.54	98.67	89.48	93.85
	ResNet+ResNet-CBAM	95.40	98.51	91.49	94.87
	<i>plain</i> -CNN+ResNet+ResNet-CBAM	95.10	97.44	91.90	94.59
128 ms	<i>plain</i> -CNN+ResNet	95.50	99.37	90.92	94.96
	<i>plain</i> -CNN+ResNet-CBAM	95.53	99.24	91.09	94.99
	ResNet+ResNet-CBAM	96.07	99.07	92.41	95.63
	<i>plain</i> -CNN+ResNet+ResNet-CBAM	95.96	99.13	92.13	95.50
64 ms	<i>plain</i> -CNN+ResNet	96.44	98.84	93.45	96.07
	<i>plain</i> -CNN+ResNet-CBAM	96.71	98.97	93.91	96.37
	ResNet+ResNet-CBAM	96.60	98.67	93.96	96.26
	<i>plain</i> -CNN+ResNet+ResNet-CBAM	96.81	98.85	94.25	96.50

NOTE—Bolded text indicates that the model performs best on that metric.

Table 4. Matching results of our searched events compared with Fermi/GBM published events.

Event	Our	Fermi	Searched Rate (%)
GRB	186	190	97.89
SFLARE	31	55	56.36
SGR	89	173	51.45
LOCLPAR	21	45	46.67
UNCERT	6	36	16.67
TGF	0	74	0
SubGRB	8(9*)	11	72.73(81.81*)
SubTrigger	64(184*)	642	9.96(28.66*)
Unknown	1558	-	-

NOTE—The LOCLPAR, SFLARE, SGR, TGF and UNCERT events are the candidates corresponded to the Fermi triggers, see (Narayana Bhat et al. 2016) for the specific definition of these triggers. The SubGRB and SubTrigger denote sub-threshold GRBs and sub-threshold triggers published by Fermi/GBM, respectively. The * indicates that only the GRB feature on a single detector matches the event. The unknown events indicate that these candidates are unable to match known events of Fermi.

Table 5. Comparison of the other unknown GRBs find by our model and various instrument.

GRB name	GCN number	Start of T_{90} (UTC)	T_{90} (s)	SNR (σ)	Detectors (n0-nb)
GRB210708B	30417(Swift/BAT)	13:23:05.320288	29.57	10.3	n3,n4,n7,n8
GRB210724A	30497(Swift/BAT)	20:14:02.903808	24.26	15.4	n9,na
GRB210930A	30897(Swift/BAT)	02:46:59.416032	7.17	10.7	n0,n1,n2
GRB220308A*	31716(Swift/BAT), 31723(Konus-Wind), 31733(AGILE)	05:43:09.182368	16.19	525.5	n0-nb
GRB220403C*	31824(Swift/BAT), 31907(Konus-Wind)	10:13:53.125568	11.90	337.5	n0-n5,n9,na,nb
GRB210820A	30664(Swift/BAT)	-	-	-	n9
GRB210822A	30677(Swift/BAT), 30678(GECAM), 30694(Konus-Wind)	-	-	-	n6
GRB211022A	30955(GECAM), 30968(AstroSat CZTI)	-	-	-	n8
GRB211025A	30986(Swift/BAT)	-	-	-	n3
GRB211107B	31057(Swift/BAT), 31086(Konus-Wind)	-	-	-	n6
GRB211218A	31261(MAXI/GSC)	-	-	-	n2
GRB220117B	31468(Swift/BAT)	-	-	-	n8
GRB220219B	31646(Konus-Wind)	-	-	-	n2
GRB220302A	31661(Swift/BAT)	-	-	-	n1
GRB220310A	31725(MAXI/GSC), 31748(Konus-Wind)	-	-	-	na
GRB220404A	31828(Swift/BAT)	-	-	-	n1
GRB220412A	31881(Swift/BAT)	-	-	-	n8
GRB220506A	32057(Konus-Wind)	-	-	-	n3
GRB220514B	32046(MAXI/GSC), 32056(Konus-Wind)	-	-	-	n6
GRB220519A	32073(Konus-Wind)	-	-	-	n2
GRB220623A	32243(Swift/BAT), 32246(AstroSat CZTI), 32258(Konus-Wind)	-	-	-	n1

NOTE— Matching results of our searched events compared with GRBweb and GCN circular published GRBs which not listed in Fermi/GBM catalog.

*The trigger time of the two GRBs, GRB220308A and GRB220403C, are close with GRB220308233 and GRB220403424, respectively. Perhaps they are the same burst probably.

Table 6. The bursts of SGR J1935+2154 in various researches and the comparison result.

Time	Lin ^a	Lin ^b	Zou ^c	Ibrahim ^d	Xie ^e
07/05/2014-08/27/2016	112	-	72	-	-
10/04/2019-05/21/2020	-	148	152	-	-
05/21/2020-07/01/2021	-	-	23	-	-
07/01/2021-09/09/2021	-	-	11	-	-
09/09/2021-10/01/2021	-	-	90	79	-
10/01/2021-10/12/2021	-	-	5	-	-
11/07/2021-01/18/2022	-	-	-	-	145
01/18/2022-06/30/2022	-	-	-	-	-
matched with Fermi trigger	62	44	167	67	67
matched with Fermi subTrigger	-	-	8	2	10
matched with our unknown events	-	-	15	7	12

NOTE— The time periods and bursts number in such different periods are shown in columns of the first two part. The corresponding literatures are ^a Lin et al. (2020b), ^b Lin et al. (2020a), ^c Zou et al. (2021), ^d Ibrahim et al. (2023), ^e Xie et al. (2022). A lot of bursts are overlapped in same period, such as Lin et al. 2020a and Zou et al. 2021. The third part represents the matched number of Fermi triggers and subTriggers with those articles in 5 second interval. The last row shows the number of those published bursts that confirms our unknown events. Of the 34 matched bursts, 10 events are overlapped.

Table 7. The comparison result of the bursts found by our model and referred researches from SGR J1935+2154.

ID	Zou ^a	Ibrahim ^b	Xie ^c	Start of T_{90} (UTC)	T_{90} (s)	SNR (σ)	RA (deg)	Dec (deg)	err (deg)	Detectors (n0-nb)
210805A	Y	N	N	00:08:55.888314	0.19	162.7	296.2	24.3	0.8	n3,n4,n6,n7,n8,nb
210910A	Y	N	N	01:04:32.065138	2.37	9.6	297.8	22.9	9.2	n6,n7
210910B	Y	N	N	01:08:40.337138	2.75	18.5	294.4	27.0	4.3	n6,n7,n9,na
210910C	Y	Y	N	01:17:18.993138	0.19	86.8	295.7	24.9	1.0	n0,n1,n6,n9,na,nb
210910D	Y	Y	N	01:18:53.505138	1.15	19.9	295.7	23.9	2.9	n1,n6,n9,na
210910E	Y	N	N	01:21:48.321138	1.28	16.9	297.0	19.6	2.7	n0,n1,n6,n9,na,nb
210910F	Y	N	N	01:31:39.921138	0.45	30.3	296.3	16.5	2.6	n9,na,nb
210910G	Y	N	N	01:34:18.737138	0.26	48.6	299.1	19.0	1.9	n9,na,nb
210910H	Y	Y	N	02:44:34.017352	0.19	93.6	295.8	26.4	1.4	n4,n6,n7,n9,na,nb
210911A	Y	N	N	17:10:48.320750	0.90	28.4	300.3	14.5	3.0	n9,na,nb
210911B	Y	Y	N	20:13:40.400030	0.26	75.1	296.2	13.8	2.1	n1,n9,na
210911C	Y	Y	N	15:06:43.169002	0.38	476.4	293.9	23.1	0.6	n1-nb
210911D	Y	Y	N	15:17:45.217002	0.38	305.7	300.3	16.9	0.6	n0-n8,na,nb
210911E	Y	Y	N	15:32:33.345002	0.32	74.5	297.9	15.8	1.3	n0,n1,n6,n9,na,nb
210911F	Y	N	N	15:34:39.793002	3.71	16.6	302.6	21.0	5.1	n9,na
220112A	N	N	Y	01:08:01.457448	0.26	102.7	295.3	19.6	1.7	n0,n1,n3,n4,n5
220112B	N	N	Y	18:12:02.256072	2.75	9.0	287.0	17.8	10.8	n0,n1,n2,n5
220113A	N	N	Y	08:34:19.666714	0.58	6.2	305.9	27.7	2.7	n1,n7
220113B	N	N	Y	15:13:21.088072	5.06	8.3	293.8	14.3	10.6	n0,n3
220114A	N	N	Y	20:46:32.873062	0.45	73.0	301.3	27.5	2.3	n1,n2,n5
220115A	N	N	Y	08:25:55.152818	1.54	71.1	293.5	18.0	1.5	n0-n7,na
220115B	N	N	Y	08:45:40.592818	0.13	105.8	299.2	21.5	1.6	n1,n3,n4,n5
220115C	N	N	Y	13:13:05.280634	3.39	15.3	290.3	21.4	5.3	n0,n3
220115D	N	N	Y	19:19:45.936170	0.19	20.3	297.4	25.1	5.3	n0,n1

NOTE— The first column is the id we compiled for the SGR event. The corresponding literatures are ^a Zou et al. (2021), ^b Ibrahim et al. (2023), ^c Xie et al. (2022). The calculations of T_{90} and SNR are shown in Appendix B. The localization algorithm is presented in Appendix C. We use the localization error within 1σ as the equivalent radius of the position region, see column ‘err’. The last column represents the detectors where our model find that the burst feature matched the trigger time of the SGR.

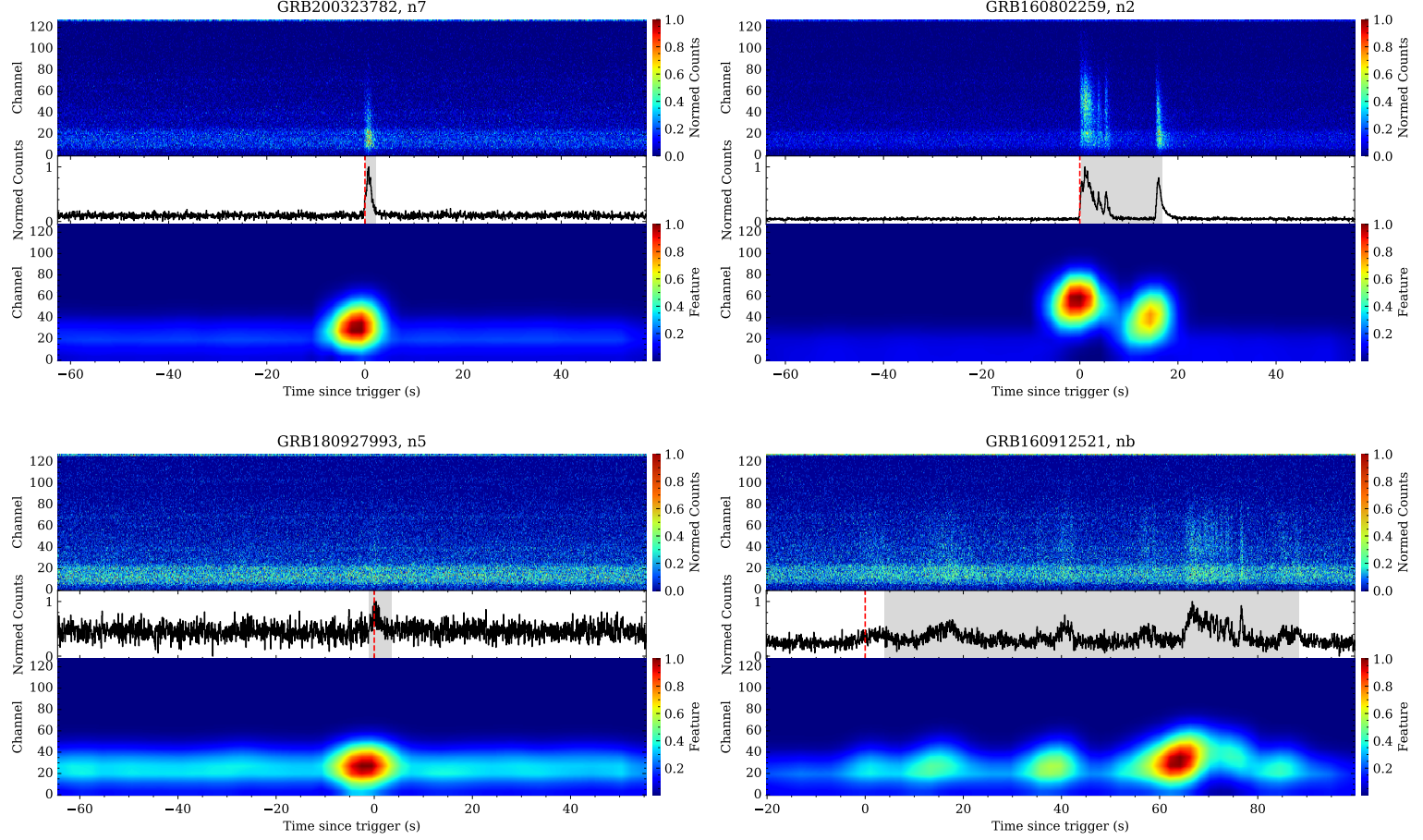


Figure 1. Four representative samples from the data set. The GRBs with single peak (GRB200323782, n7), two peak (GRB160802259, n2), low SNR (GRB180927993, n5), and complex structure (GRB160912521, nb) are represented. For each sub-figure, the top panel shows the normalized count map (model input), the central panel shows the normalized light curve of full energy band, while the bottom panel is the feature heat-map generated by Grad-CAM method. The red dashed line represents the trigger time of Fermi and the gray area indicates the Fermi- T_{90} .

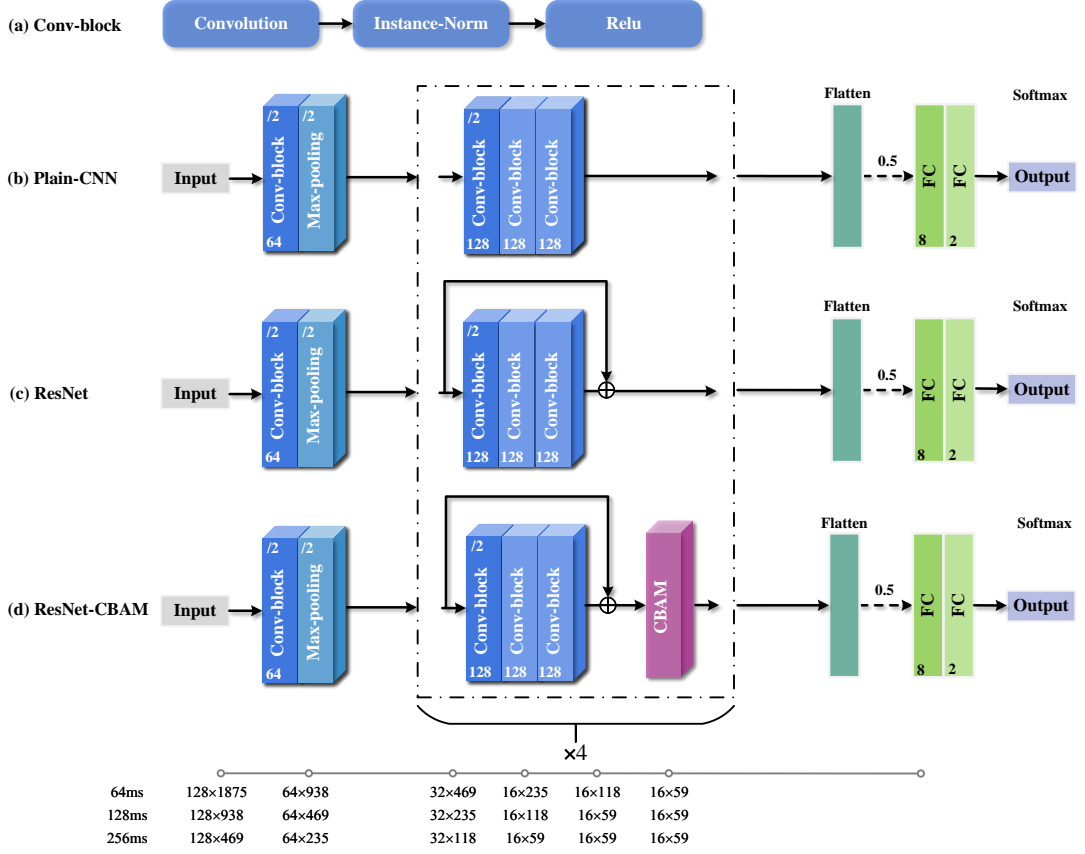


Figure 2. Schematic diagram of our CNN architectures. The numbers at the top and bottom of Conv-block denote the convolutional stride (default is 1) and number of convolutional kernels, respectively. The number at the bottom of the figure describes the variation of the length and width of the feature maps.

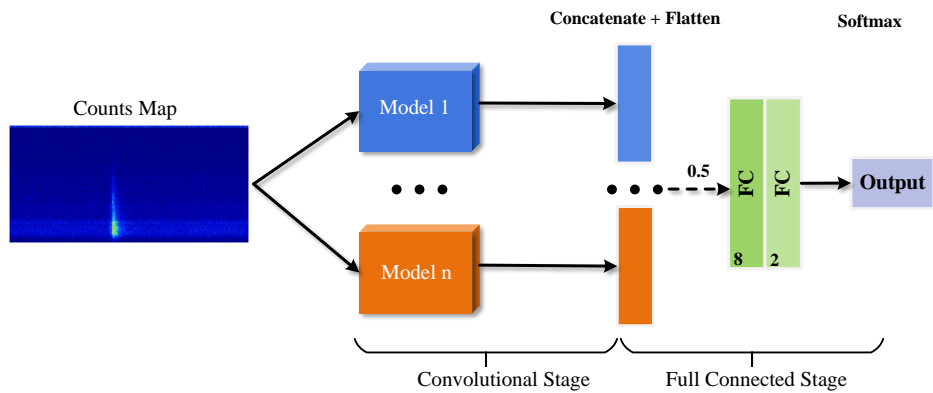


Figure 3. Overall architecture of fused model.

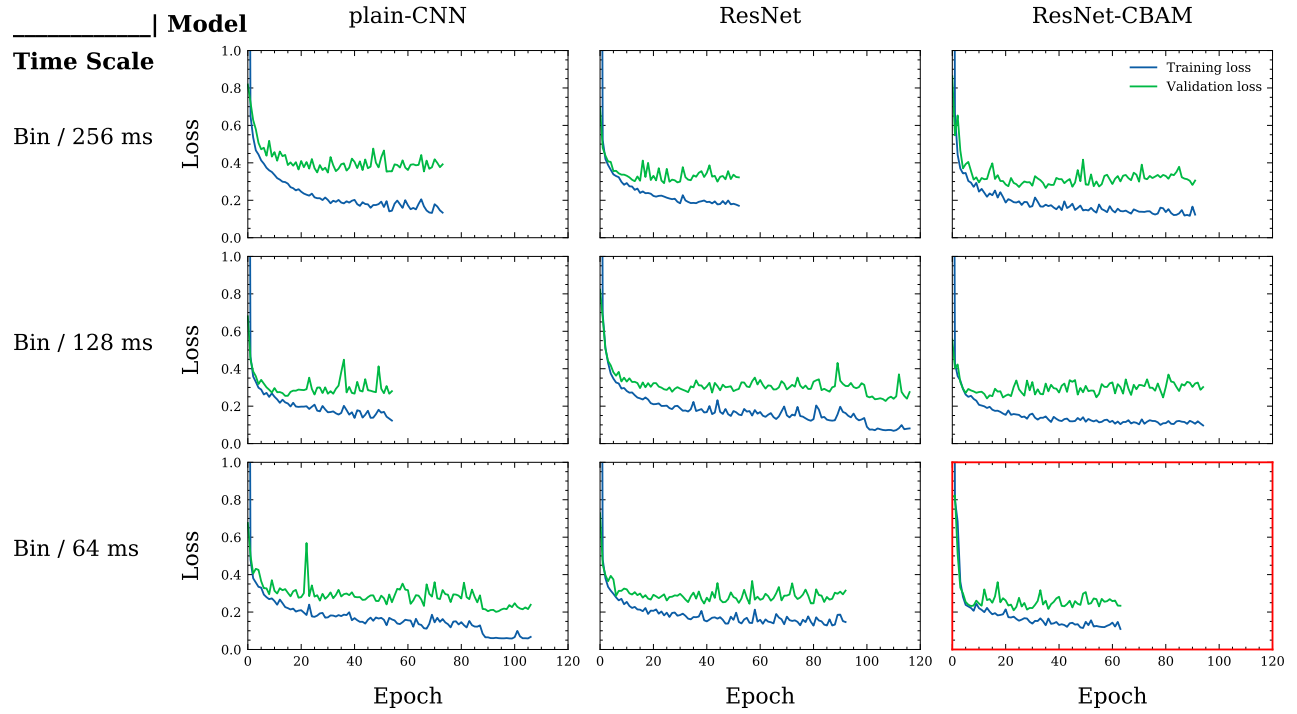


Figure 4. The learning curve of nine single network models. Due to the training mechanism of early stopping, the epoch at which the model stops varies.

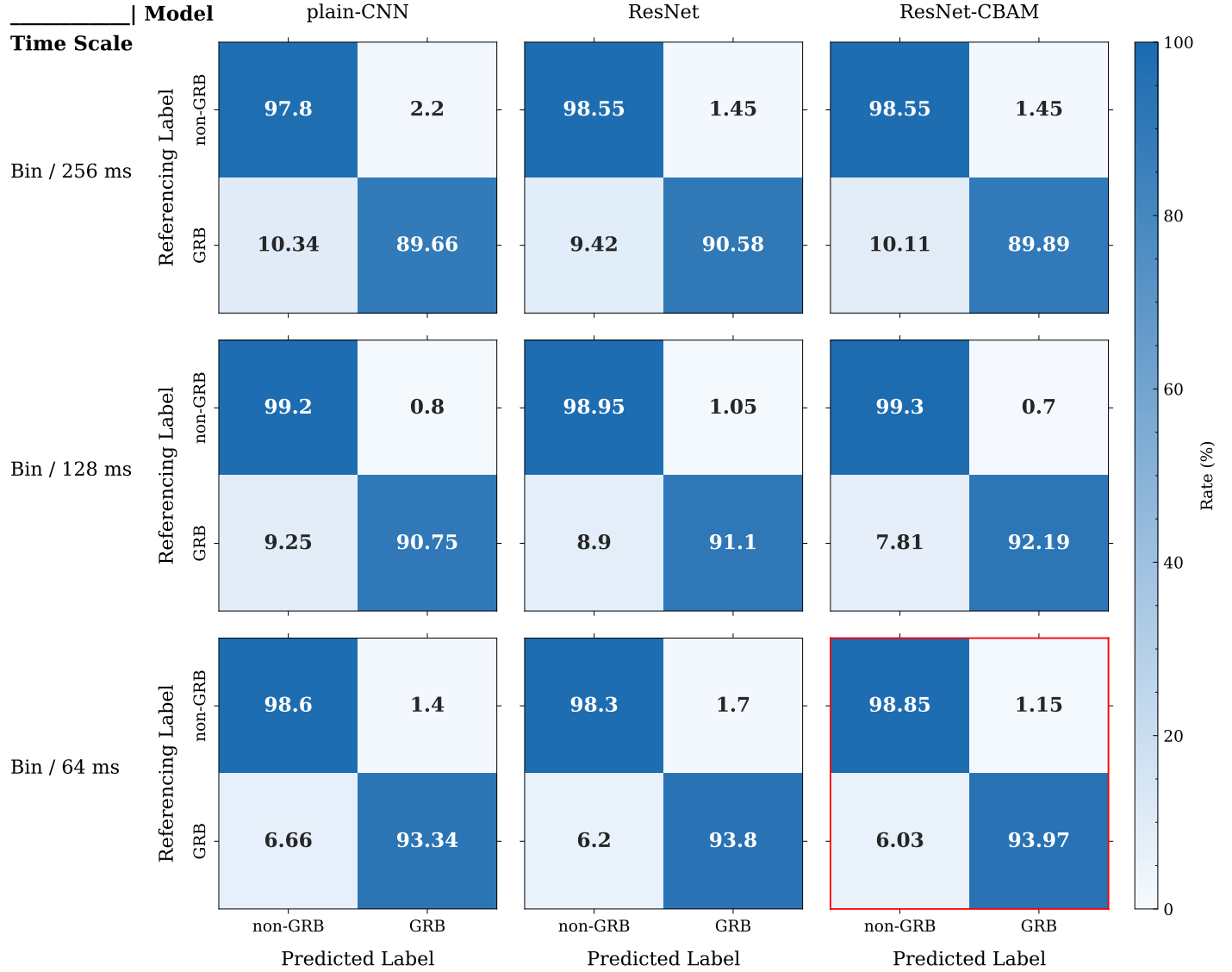


Figure 5. The confusion matrices of nine single network models.

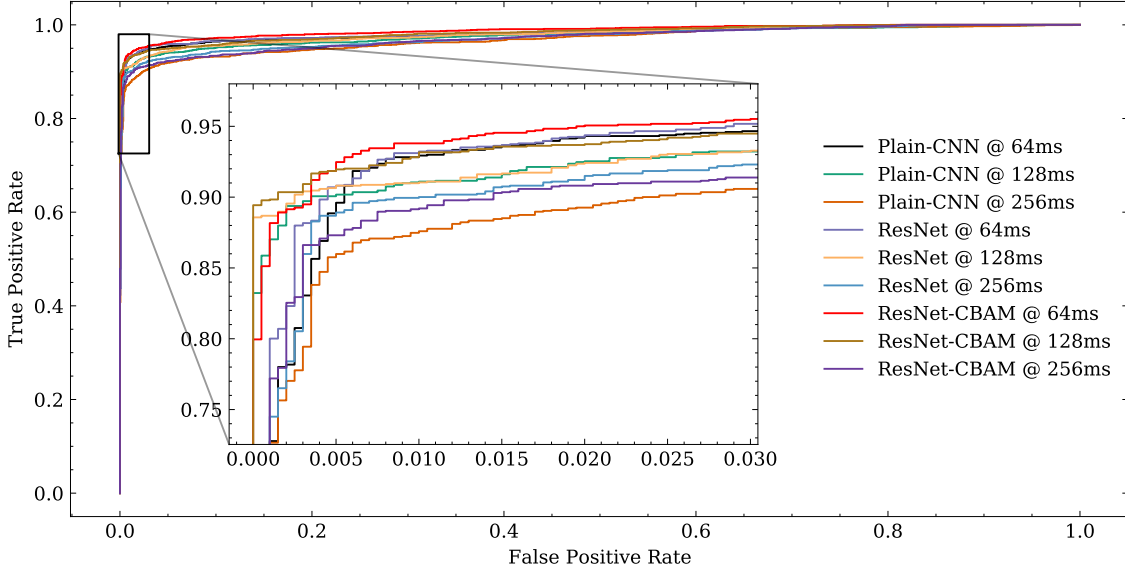


Figure 6. The ROC curves depicts the True Positive Rate ($\frac{TP}{TP+FN}$) versus the False Positive Rate ($\frac{FP}{FP+TN}$).

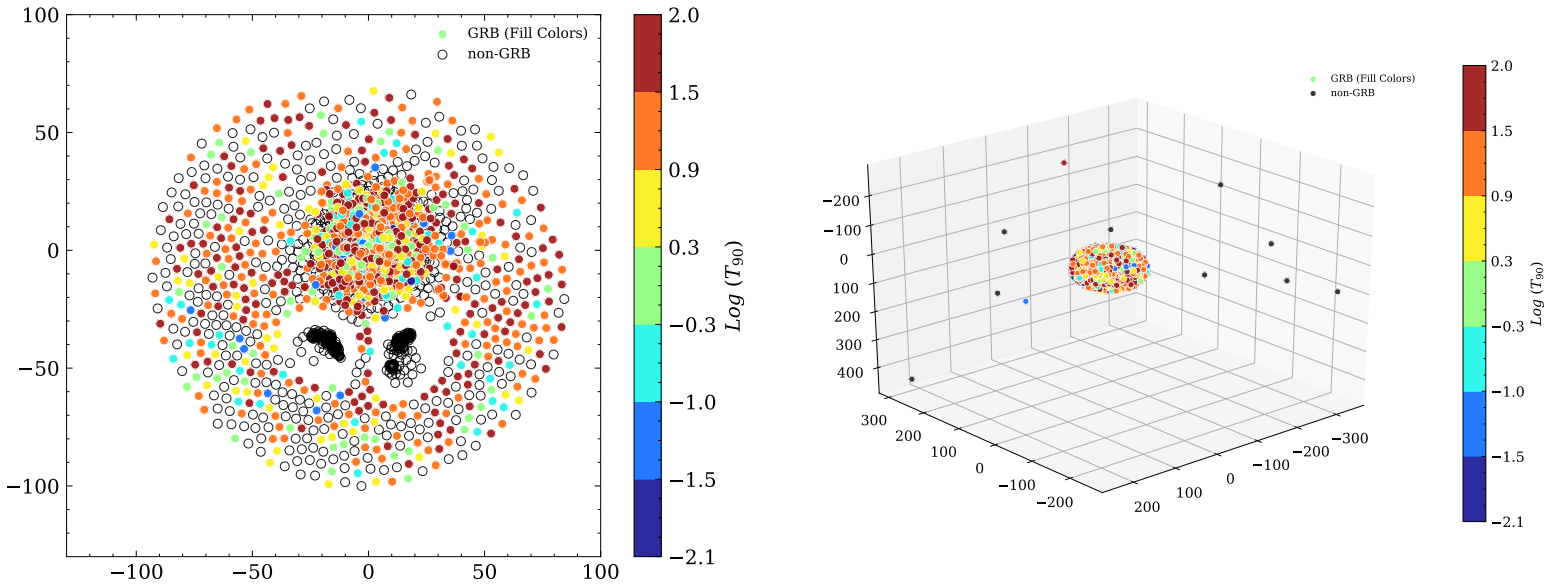


Figure 7. The 2D and 3D visualization of the count maps is achieved using the dimensionality reduction method t-SNE, with T_{90} information embedded for each sample. The count maps are the samples in the test set without normalized preprocessing. The T_{90} of each GRB sample is derived from the corresponding GRB in the Fermi burst catalog. It is not able to calculate the duration of the non-GRB samples. The distributions of primary count maps in feature space for GRB and non-GRB category are indistinguishable.

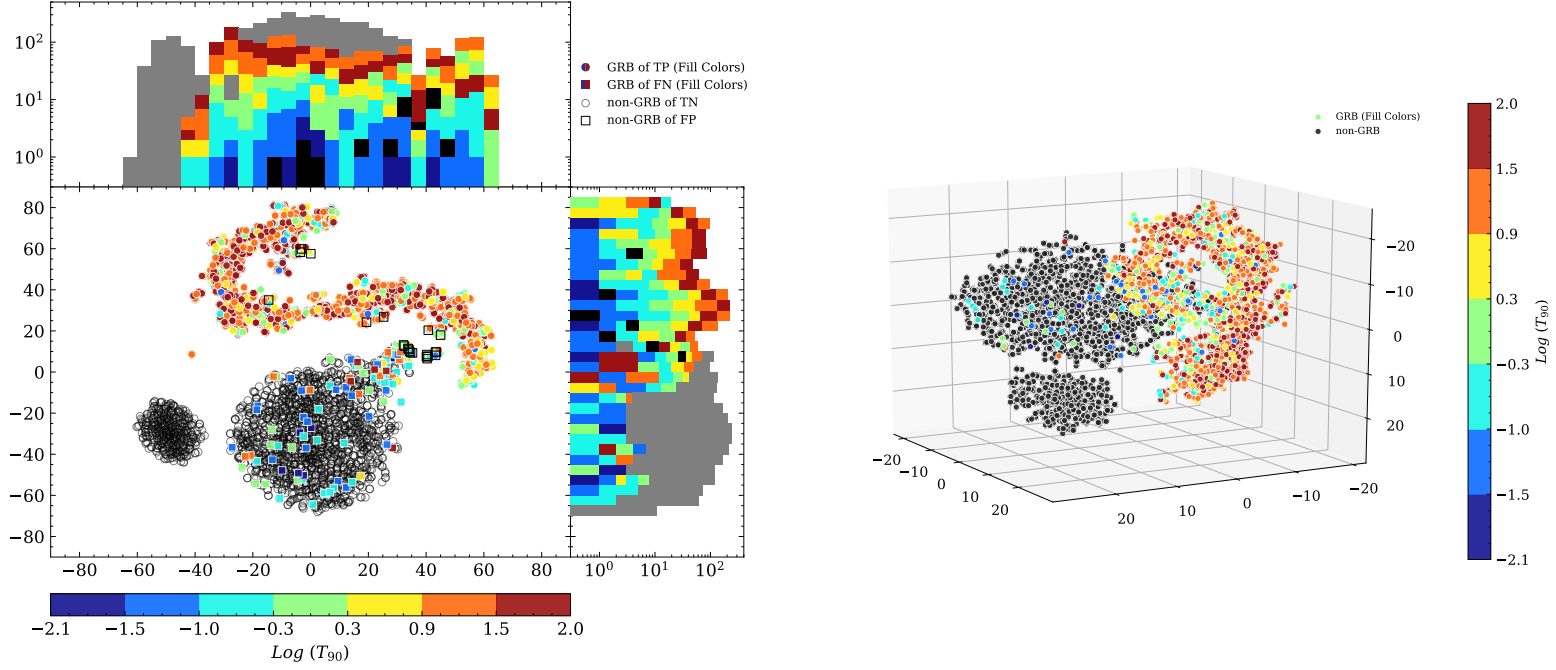


Figure 8. The 2D and 3D visualization of the feature maps is achieved using the dimensionality reduction method t-SNE, with T_{90} embedded for each sample. The feature maps are output by the last convolutional layer of optimal model on test set. The distributions of feature maps in feature space for GRB and non-GRB category are indistinguishable. The feature maps of GRB and non-GRB categories show a clear aggregations. The duration of the GRB of FN samples was relatively short.

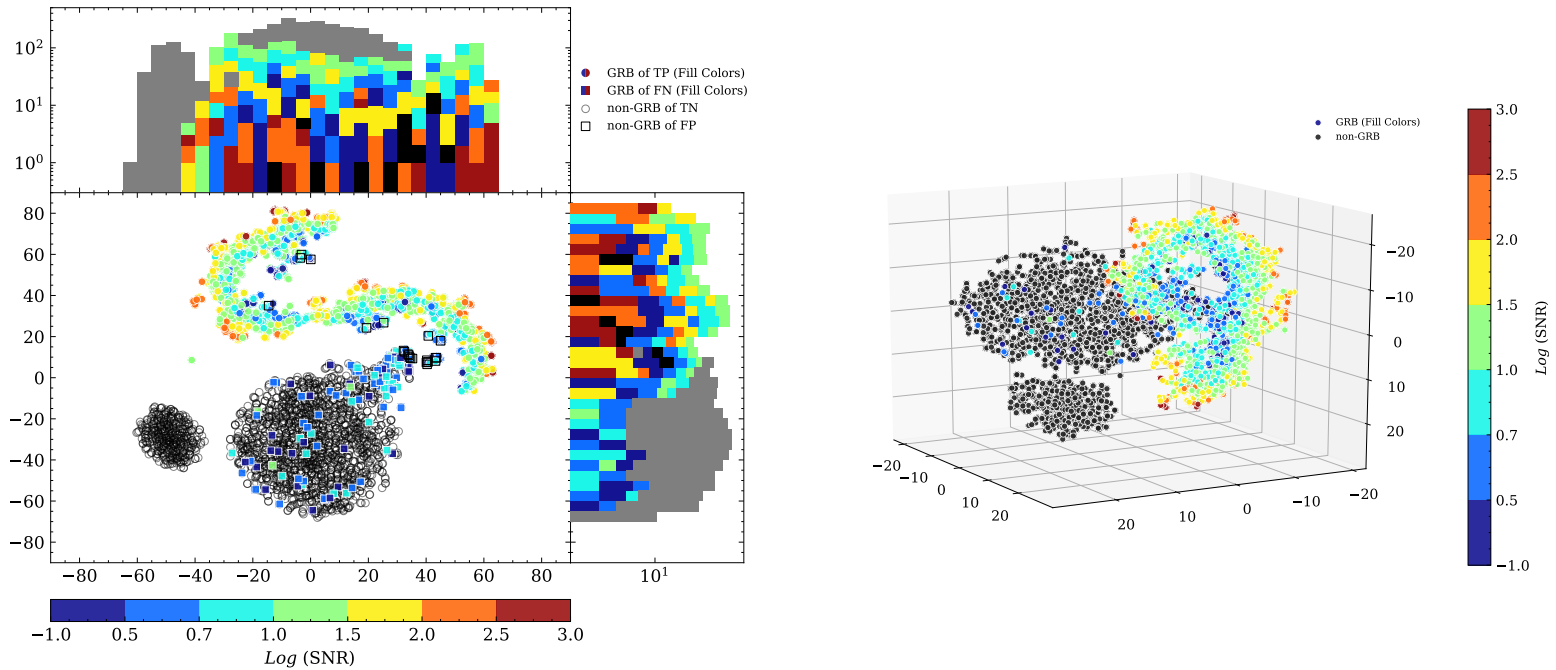


Figure 9. The 2D and 3D visualization of the feature maps is achieved using the dimensionality reduction method t-SNE, with SNR (calculation see Appendix B) embedded for each sample. The SNR of the GRB of FN samples was relatively low.

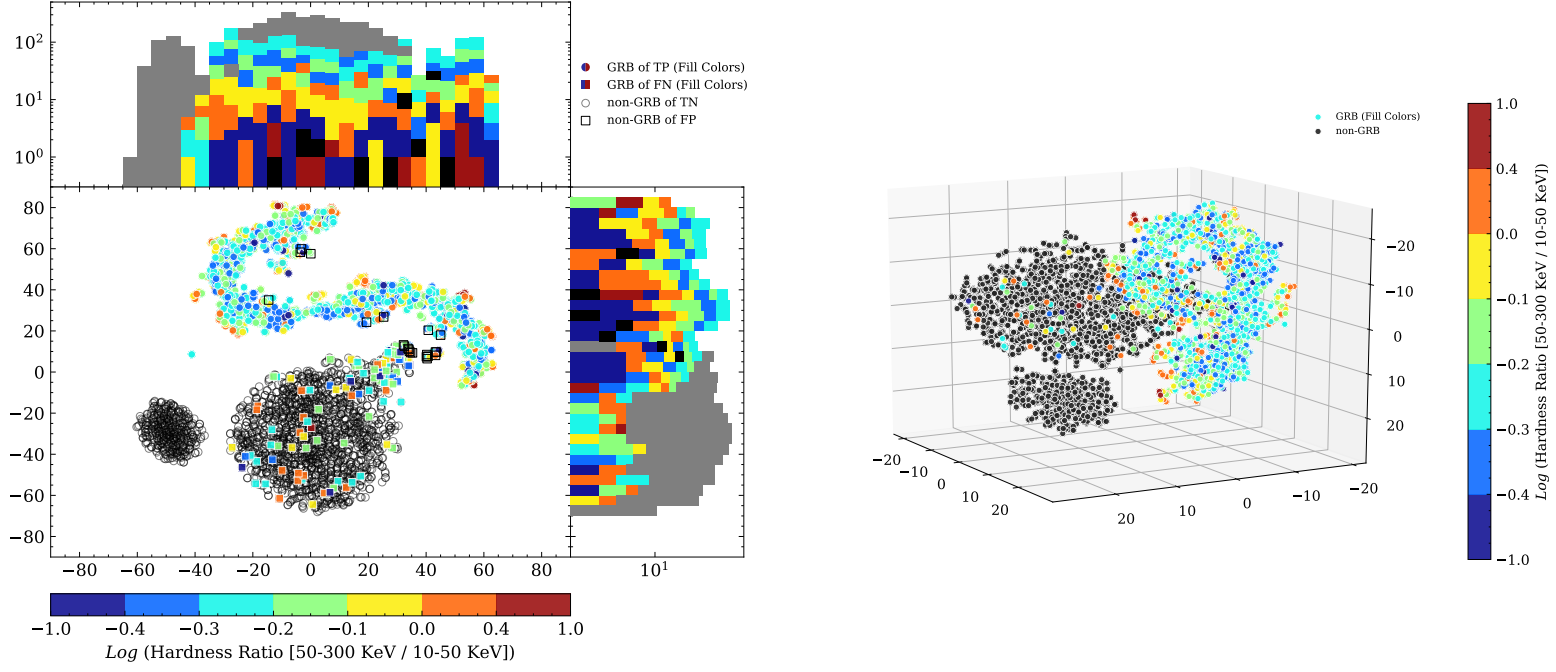


Figure 10. The 2D and 3D visualization of the feature maps is achieved using the dimensionality reduction method t-SNE, with hardness ratio embedded for each sample. There is no clear pattern is found in the hardness ratio of the GRB of FN samples.

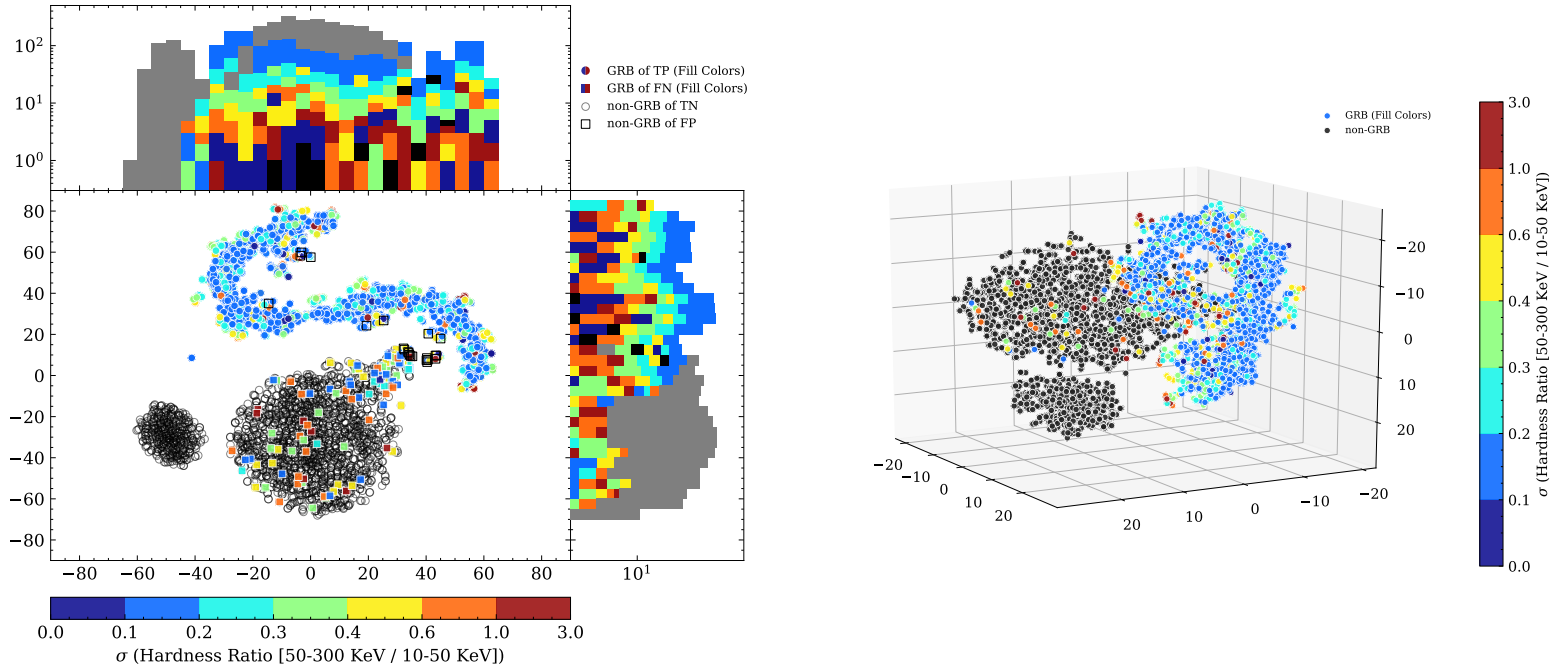


Figure 11. The 2D and 3D visualization of the feature maps is achieved using the dimensionality reduction method t-SNE, with standard deviation of the hardness ratio embedded for each sample. The SNR of the GRB of FN samples was relatively low. The dispersion of GRB hardness ratios for FN samples is relatively large.

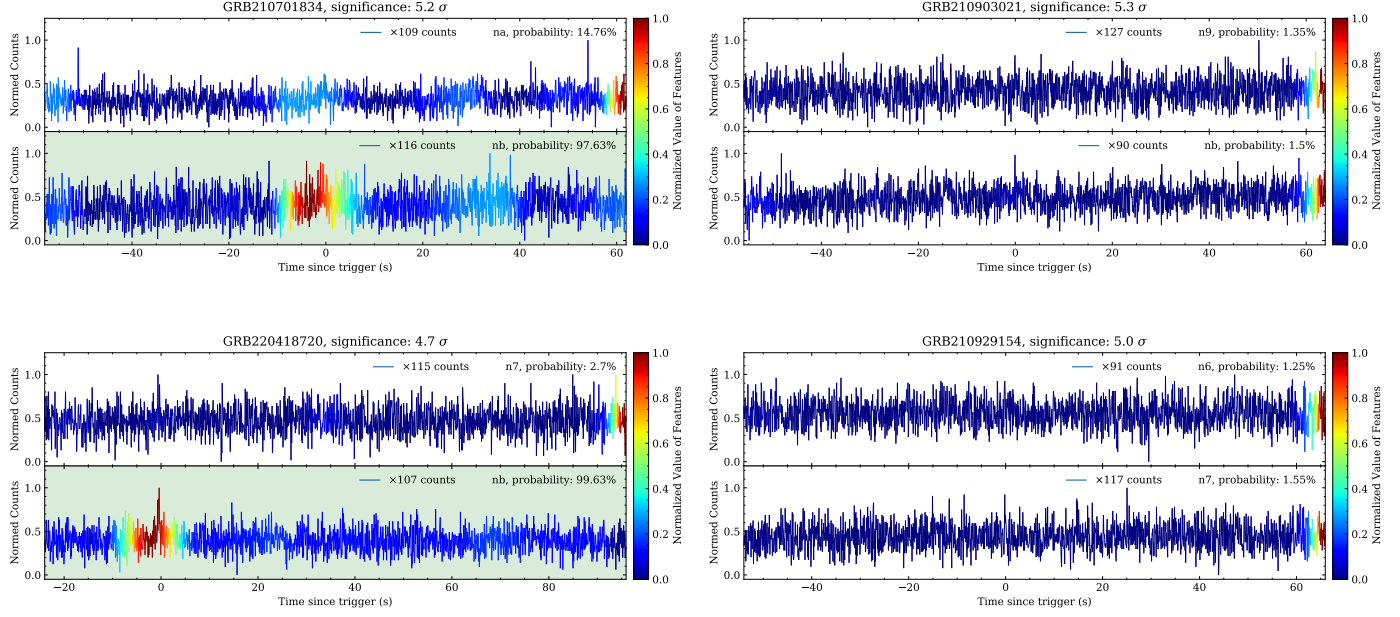


Figure 12. The mapping-curves of the 4 GRBs that our model failed to identify. The green background indicates the model distinguished the burst signal. The time of the curve is relative to the trigger time of Fermi/GBM. The significance are derived from the TRIGDAT file of GBM burst data products.

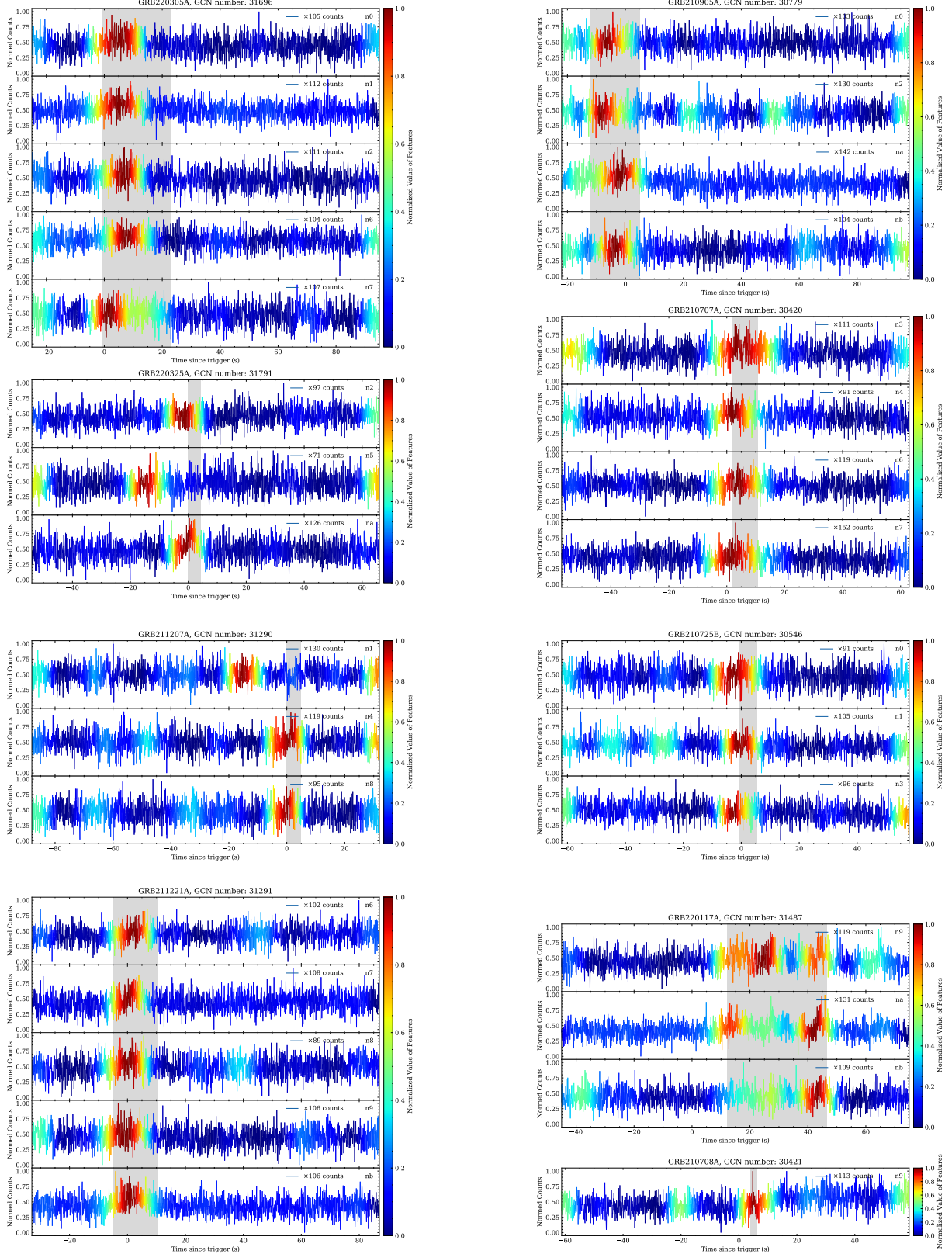
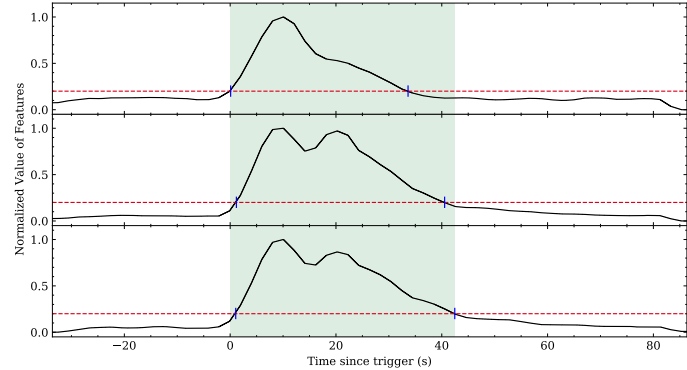
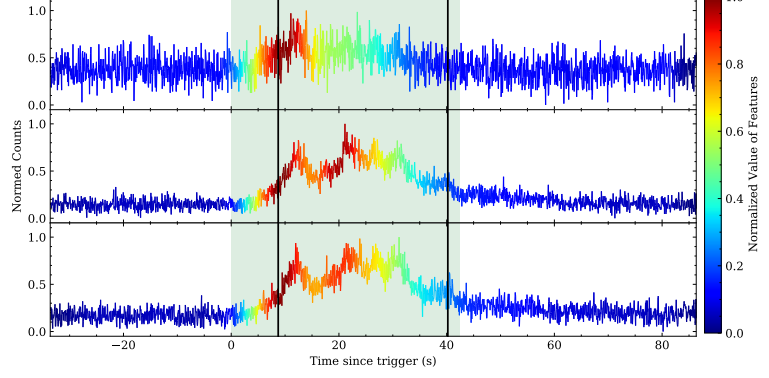


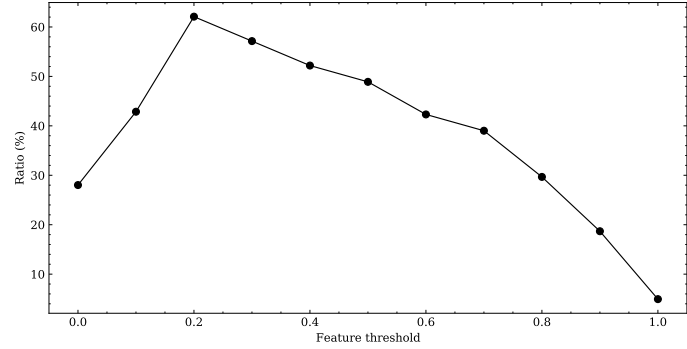
Figure 13. The mapping-curves of seven sub-threshold GRBs (GCN circular) that our model identified. The symbol * indicates that the model distinguished the burst signal on only one detector. The time of the curve is relative to the trigger time in the GCN. The gray period is T_{90} , and its calculation method is shown in the Appendix B.



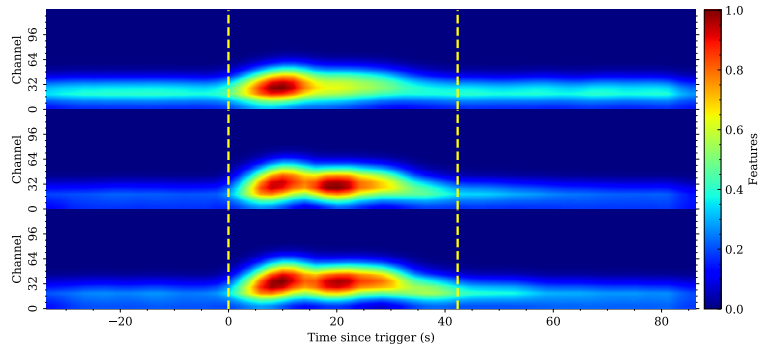
(a)



(b)



(c)



(d)

Figure 14. Right: the heat-map of feature and the mapping-curves of feature. Left: curve obtained by summing the heat-map of feature along channel dimension and the IoU (Fermi- T_{90} and $T_{90,F}$) are > 0.3 with various feature thresholds from the identified GRBs in Section 4.2. The red dashed lines are the set feature threshold. The green area represents the period of $T_{90,F}$. The black vertical line indicates the Fermi- T_{90} .

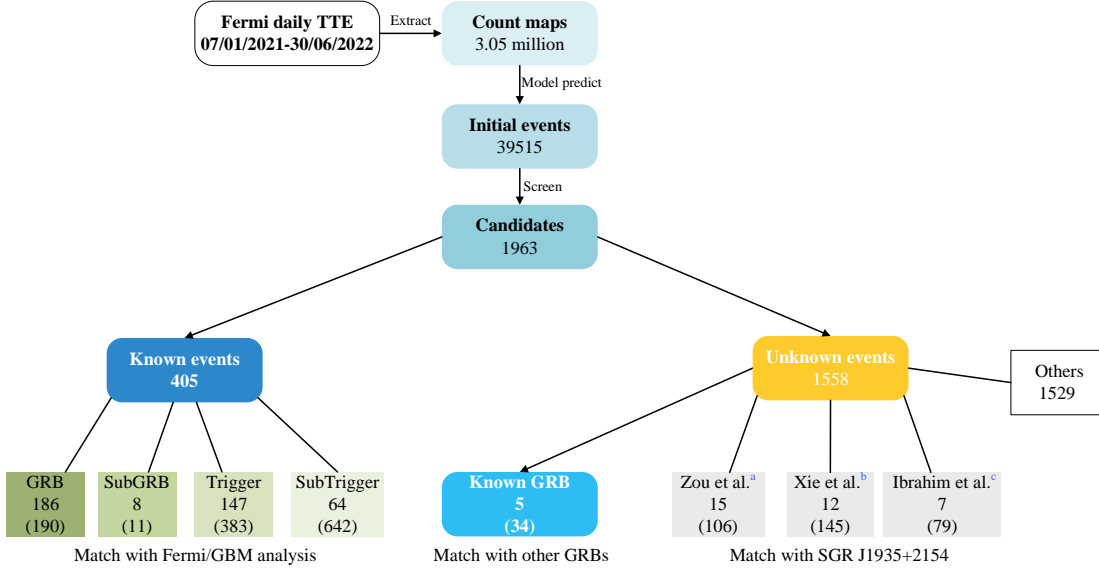


Figure 15. The process of our searching method, and the matching result. We compared our 1963 candidates with events that existed in Fermi catalogs and literatures, ^a Zou et al. (2021), ^b Xie et al. (2022), ^c Ibrahim et al. (2023). The number in parentheses present the published bursts in total. There are 1536 candidates left, shown as 'Other', which indicates the nonmatched events. These results are corresponding to Table 4 and Table 6.

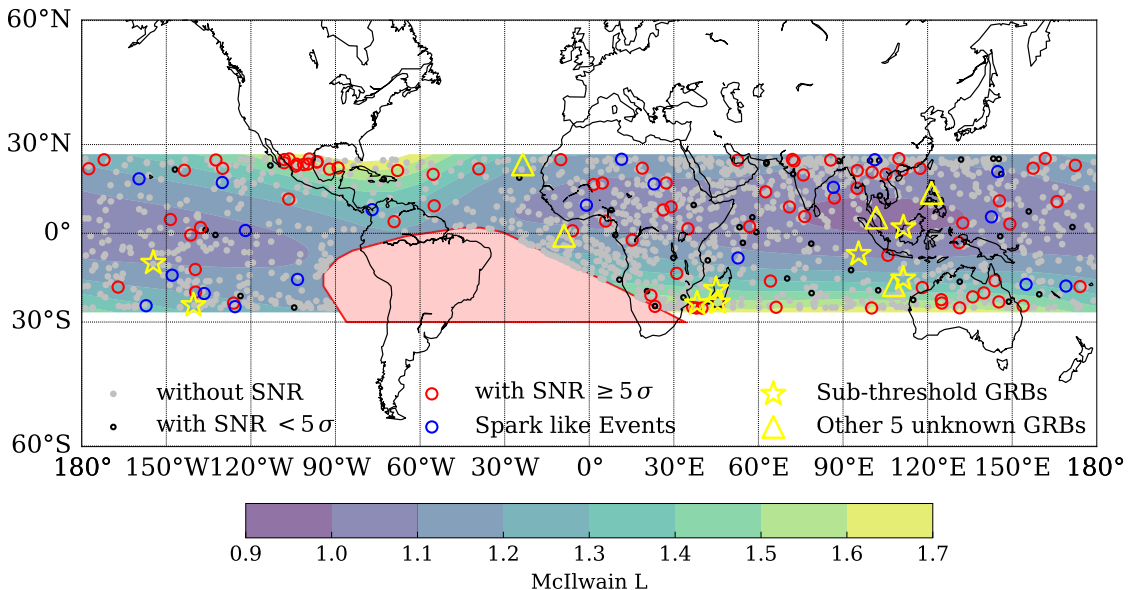


Figure 16. Location of the Fermi spacecraft in orbit at the $T_{90,F}$ start time of the candidates. The color gradient shows the geomagnetic latitude according to the McIlwain L. If the spacecraft is in the region where the McIlwain L is greater than 1.5, the candidate is likely to be associated with local particles.

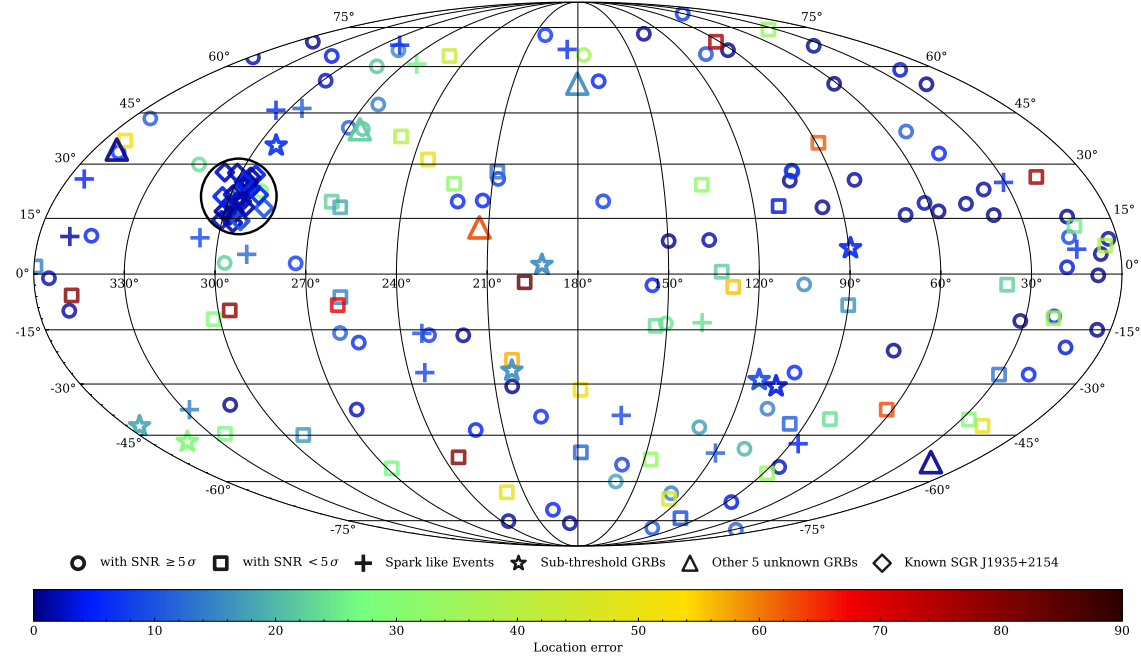


Figure 17. The localization of the unknown events. The color bar illustrates the localization error of events within 1σ equaled to the radius of spatial position error. The thick black circle encloses the events from SGR J1935+2154.

Table 8. Candidates with $\text{SNR} \geq 5\sigma$ of unknown events.

Can.ID	Start of $T_{90,F}$ (UTC)	$T_{90,F}$ (s)	Start of T_{90} (UTC)	T_{90} (s)	SNR (σ)	RA (deg)	Dec (deg)	err (deg)	Can.ID	Start of $T_{90,F}$ (UTC)	$T_{90,F}$ (s)	Start of T_{90} (UTC)	T_{90} (s)	SNR (σ)	RA (deg)	Dec (deg)	err (deg)
210702A	00:23:44.208415	20.03	00:23:51.120406	11.90	17.7	221.2	19.6	5.6	220306B	07:57:16.097252	25.66	07:57:30.753246	11.46	10.5	108.1	64.4	9.8
210703F	06:29:43.865561	58.43	06:29:50.777554	44.93	9.0	16.1	9.9	8.5	220309B	10:23:18.833991	15.42	10:23:20.497976	16.58	6.7	342.5	10.3	5.0
210706C[®]	21:48:30.000608	42.50	21:48:39.792608	49.47	74.1	105.4	25.4	0.6	220309E	22:06:20.736690	34.50	22:06:33.536680	16.96	5.6	282.9	60.1	21.1
210710D[†]	23:41:57.677494	16.26	23:42:07.725490	0.19	36.0	295.5	21.0	3.3	220310A[*]	03:00:56.816929	17.34	03:00:42.480918	30.85	46.6	136.2	9.1	1.9
210718A[†]	02:16:39.776219	32.77	02:16:57.056216	0.19	14.3	14.3	6.7	6.7	220311F[•]	18:29:56.893393	26.11	18:30:01.373382	22.40	5.5	290.0	22.5	29.6
210720G[†]	13:19:10.001086	25.73	13:19:28.241086	0.19	13.7	234.3	-26.8	8.6	220313B[®]	04:13:32.545743	20.35	04:13:36.321734	16.70	41.3	354.9	-1.1	2.1
210728B[•]	01:43:18.432015	16.00	01:43:28.736012	0.32	9.0	30.5	24.9	6.8	220314A[•]	01:09:18.048336	41.66	01:09:22.912336	40.38	36.7	92.7	65.9	0.6
210807D	23:37:41.392846	61.95	23:37:44.592846	30.46	8.6	61.2	81.6	7.5	220314C[•]	02:46:49.057621	41.09	02:47:10.881610	17.86	6.3	150.4	-13.3	24.8
210808F[•]	13:04:49.6680125	30.78	13:04:55.947212	19.71	5.3	176.7	64.1	35.9	220314D	06:46:31.009102	68.93	06:46:55.009094	40.06	96.1	133.6	72.3	0.8
210817C[†]	17:05:36.434855	15.42	17:05:46.290844	0.26	11.5	328.1	-37.4	14.4	220315B[•]	05:09:41.283279	32.26	05:09:50.755272	0.77	6.6	27.4	-79.2	11.6
210820C[®]	15:46:59.648119	40.58	15:47:15.712116	58.43	291.4	149.8	8.9	0.6	220325C	21:02:33.504505	25.54	21:02:36.832496	30.14	9.1	269.8	40.5	11.5
210830C	11:53:14.513261	55.42	11:53:18.545250	43.52	51.6	36.8	67.5	1.4	220326F[•]	08:24:10.087481	16.26	08:24:15.079478	17.73	5.4	160.7	-60.0	17.7
210830E	13:32:48.064850	71.87	13:32:55.104842	44.16	29.5	316.0	63.7	3.7	220326I	08:50:21.383486	15.62	08:50:25.479478	15.04	5.5	131.4	-42.6	17.2
210909D[†]	20:31:09.969226	21.57	20:31:26.097226	0.13	10.1	289.8	5.3	12.4	220326J	23:20:47.808246	20.10	23:20:45.760238	29.06	6.2	128.0	-64.1	14.4
210913A	02:33:24.864734	21.18	02:33:33.056720	12.61	29.5	18.8	58.9	3.0	220328B[†]	11:27:58.401066	14.85	11:28:07.873060	0.13	7.3	349.6	10.1	0.8
210925C[•]	19:15:32.177918	49.92	19:15:36.913918	43.07	54.2	349.7	-9.9	1.1	220329B[®]	07:43:12.527156	31.42	07:43:22.575154	42.18	97.2	7.9	-0.3	0.6
211030C[®]	16:21:18.006991	34.94	16:20:33.846982	69.44	106.3	203.9	-30.7	0.6	220329D[®]	17:38:38.177283	54.34	17:39:04.929280	32.77	113.7	4.6	-15.0	0.6
211101A[®]	01:32:00.001530	39.68	01:32:08.577530	24.19	28.2	218.9	-16.5	1.0	220329E[®]	20:18:58.320056	39.23	20:19:08.944048	24.19	58.0	6.6	5.4	0.8
211106A	07:13:34.656431	31.23	07:13:38.944422	28.29	14.9	20.6	-11.4	6.3	220404C[†]	09:27:21.563139	27.84	09:27:42.491136	0.13	7.2	86.9	-47.6	5.1
211109A[•]	02:47:16.784010	28.48	02:47:28.240000	12.22	15.0	264.3	-37.3	2.3	220404E[•]	19:09:41.025341	60.67	19:09:39.041334	52.35	43.3	186.6	-76.1	1.1
211113D	11:50:17.941036	22.85	11:49:42.805022	55.30	16.6	46.8	33.0	5.0	220408E[®]	19:50:10.306220	28.03	19:50:21.954212	22.59	23.0	18.2	1.8	3.2
211117C[•]	09:23:56.369239	15.42	09:24:05.841228	1.09	6.2	107.9	-37.1	14.3	220415K[•]	13:19:54.448011	55.49	13:20:04.304000	36.16	29.3	196.5	-70.4	5.2
211123C[†]	23:51:44.020750	16.00	23:51:53.748742	0.19	12.5	305.0	45.8	5.9	220415L	13:20:40.064137	37.57	13:20:31.040130	47.42	14.3	170.3	55.1	5.1
211127A	22:36:09.373706	33.60	22:36:15.389696	27.90	12.7	254.9	-18.5	6.2	220417A	06:51:27.088593	41.47	06:51:52.240590	26.94	9.5	349.9	33.4	7.7
211130E	09:13:03.985470	45.95	09:13:01.233458	40.45	19.8	208.1	25.9	7.1	220417D	22:19:21.744928	34.75	22:19:30.768916	16.13	5.1	284.3	65.9	15.2
211130F	15:19:50.192979	28.61	15:19:50.064972	29.38	17.3	19.6	-27.3	4.9	220418B[®]	07:48:16.080850	60.80	07:48:29.584842	39.62	699.4	31.5	-12.6	0.6
211205F	22:42:35.633450	18.75	22:42:31.921436	20.99	9.5	103.4	27.9	7.3	220425A[•]	08:51:44.177114	22.91	08:51:33.489108	51.46	17.6	14.5	15.5	0.6
211207B	21:34:34.815607	41.02	21:34:54.335596	17.92	15.7	357.6	63.3	1.9	220429B[•]	06:05:04.592620	25.34	06:05:14.448604	10.43	18.4	221.2	-43.4	4.7
211215A	00:08:19.9202636	54.08	00:08:38.800634	31.62	15.8	171.3	19.7	7.6	220501A[®]	00:45:57.344769	40.51	00:46:03.744766	32.70	31.0	38.8	22.9	1.3
211215B	00:13:00.272645	29.38	00:13:01.872634	22.72	15.1	155.3	-3.0	5.4	220507D[•]	20:03:53.424862	17.86	20:04:04.048858	0.13	10.4	186.3	66.2	6.6
211227A	02:51:14.890662	44.86	02:51:29.610650	20.99	12.0	202.5	71.8	7.1	220508A[®]	07:45:29.192379	34.24	07:45:36.744378	83.20	178.0	39.1	15.9	0.6
220104C	06:06:48.064196	31.87	06:06:55.040182	13.82	6.7	52.6	39.4	11.0	220510A[†]	00:51:56.481930	17.09	00:51:56.401924	0.13	10.6	163.2	-39.0	8.9

Table 8 continued on next page

Table 8 (continued)

Can.ID	Start of $T_{90,F}$ (UTC)	$T_{90,F}$ (s)	Start of T_{90} (UTC)	T_{90} (s)	SNR	RA (deg)	Dec (deg)	err (deg)	Can.ID	Start of $T_{90,F}$ (UTC)	$T_{90,F}$ (s)	Start of T_{90} (UTC)	T_{90} (s)	SNR	RA (deg)	Dec (deg)	err (deg)
220112F	14:59:29.281717	30.66	14:59:40.353702	15.10	8.4	296.9	3.0	22.4	220512A	08:13:57.569435	42.37	08:14:24.385422	9.34	7.0	111.6	-78.4	10.3
220113G[®]	17:09:59.397772	19.26	17:10:01.061760	23.55	30.8	293.8	14.3	10.6	220512B	08:16:20.001422	37.38	08:16:35.169422	17.34	11.9	87.1	-67.4	3.8
220117C	16:18:53.187612	49.79	16:19:06.499612	30.91	15.0	103.2	-26.8	5.6	220513G[†]	15:11:26.86286	15.74	15:11:37.362280	0.26	5.8	119.6	-50.6	11.5
220118E	21:30:32.170268	33.66	21:30:40.426262	15.68	10.5	260.6	-15.9	11.3	220514B[®]	14:23:59.101268	54.46	14:24:14.525268	40.19	68.4	47.2	19.0	1.0
220118G[†]	23:45:16.144900	33.79	23:45:29.648886	0.19	13.0	354.2	25.8	5.1	220515E[®]	19:50:08.770534	31.94	19:50:17.410526	25.02	73.6	57.4	16.9	0.6
220121C	03:05:52.640397	18.37	03:05:54.624392	18.11	7.7	105.1	-2.8	15.8	220522F[•]	20:58:33.538174	47.49	20:58:38.594162	30.78	44.2	71.2	-20.7	0.6
220122D[•]	10:28:07.873798	38.14	10:28:06.401790	40.26	19.5	273.4	2.9	7.9	220525A[®]	02:00:59.312143	20.74	02:00:56.240132	23.42	28.9	61.3	19.2	1.6
220125A	06:11:34.928223	33.98	06:11:44.272216	23.74	29.3	12.6	-19.8	3.2	220526A[®]	02:16:31.972740	24.90	02:16:47.140738	68.74	33.5	69.0	15.9	1.5
220125D[•]	15:07:49.553182	37.50	15:07:50.321176	32.38	6.4	316.9	29.9	23.6	220527D[†]	22:08:00.432768	20.03	22:08:09.776760	0.26	10.1	306.1	9.7	9.1
220131A	08:08:50.009097	24.26	08:09:01.081092	34.62	8.5	159.6	-54.3	8.2	220529C	12:29:29.136005	24.45	12:29:31.248002	25.22	21.2	298.5	55.2	2.7
220201A	09:33:08.000000	43.07	09:33:34.752000	13.57	5.0	247.8	38.0	39.7	220601E[†]	12:32:31.968123	18.24	12:32:42.144108	0.13	8.7	232.9	-16.0	10.0
220203A[•]	11:16:34.976676	16.32	11:16:38.944674	17.92	17.8	311.1	-36.0	0.6	220601F[•]	13:04:25.424279	39.81	13:04:23.056270	22.66	6.5	230.5	-16.5	7.1
220205A	05:21:16.023351	79.36	05:21:29.527344	17.09	17.8	234.7	-75.2	1.1	220606C	14:43:39.646134	24.26	14:43:41.502130	21.50	12.9	212.7	19.9	5.0
220205B	14:43:29.796353	30.14	14:43:40.996338	10.50	7.3	264.0	40.2	21.4	220612E	16:25:04.933174	23.68	16:25:13.509160	13.31	12.7	103.6	28.2	7.2
220205D	15:42:25.810579	30.21	15:42:30.610564	8.19	6.1	264.4	47.6	14.1	220616C[®]	13:40:56.185968	18.18	13:41:02.201954	13.44	37.1	82.5	25.6	1.4
220209I[*]	23:03:55.089014	28.54	23:04:01.553010	19.90	166.1	348.3	69.1	0.6	220620F[®]	21:38:50.080469	25.73	21:38:55.264464	24.06	65.1	96.6	18.0	0.8
220212A[•]	03:45:20.558386	95.87	03:45:53.902386	24.70	280.5	19.2	54.0	0.6	220624D[†]	18:02:19.488207	15.81	18:02:28.512200	0.13	8.8	288.9	67.8	6.0
220218A[†]	03:27:45.473694	14.85	03:27:54.561690	0.13	5.6	138.2	-13.1	24.2	220625A[•]	22:59:15.906572	44.03	22:59:16.674560	29.63	13.5	3.1	9.5	1.1
220226C[•]	11:59:21.153317	38.78	11:59:25.185304	27.78	9.0	61.5	54.2	0.6	220626A	17:46:04.128524	41.28	17:46:11.872520	25.66	5.2	108.2	-49.2	19.6
220301A	00:59:06.688237	18.62	00:59:16.032226	6.34	7.4	352.3	43.3	10.7	220627H[*]	21:25:30.000472	19.84	21:25:40.432472	5.38	20.8	194.3	-39.4	5.7

NOTE— We use the localization error within 1σ as the equivalent radius of the position region, see column ‘err’.

[†]The event is considered to be a likely spark event after manual inspection.

^{*}The event is part of a long burst.

[•]The event is located in the earth occlusion region.

[®]According to the location, the signal of the event come from the sun.

Table 9. Candidates with SNR < 5 σ of unknown events.

Can.ID	Start of $T_{90,F}$ (UTC)	$T_{90,F}$ (s)	Start of T_{90} (UTC)	T_{90} (s)	SNR (σ)	RA (deg)	Dec (deg)	err (deg)	Can.ID	Start of $T_{90,F}$ (UTC)	$T_{90,F}$ (s)	Start of T_{90} (UTC)	T_{90} (s)	SNR (σ)	RA (deg)	Dec (deg)	err (deg)
210701A	19:34:57.841309	24.06	19:35:10.129298	9.79	3.9	96.1	-41.6	11.2	211204A[†]	03:37:21.798223	17.22	03:37:33.766212	0.13	2.4	295.0	46.4	11.0
210703B	01:21:26.414169	21.44	01:21:35.182160	7.68	4.7	359.4	2.0	14.1	211208D	16:32:38.046245	14.66	16:32:45.918242	4.86	3.7	324.2	-44.6	27.0
210711A	03:08:21.840390	28.80	03:08:30.756388	9.79	2.9	13.2	12.9	25.1	211213D[•]	18:39:03.247260	29.50	18:39:19.951260	6.85	4.3	234.6	31.3	50.1
210713D[•]	19:22:53.313285	36.48	19:23:16.353282	2.94	4.7	81.5	-40.1	24.1	211216D[•]	16:59:06.048041	42.30	16:59:08.800030	25.66	4.6	258.8	-6.2	14.7
210717E	23:46:54.655941	27.97	23:47:04.831940	4.80	3.1	351.8	36.8	53.4	211222C	12:14:10.848777	25.28	12:14:08.416772	24.77	4.3	153.8	-13.9	23.7
210720A[•]	02:58:04.383355	19.33	02:58:13.983344	7.17	4.2	208.7	27.9	13.2	211222E[•]	14:27:48.160643	46.66	14:27:56.416638	3.26	3.7	89.2	36.1	61.9
210720B	03:12:46.833447	27.97	03:12:52.017438	10.94	4.4	126.5	-66.2	45.9	211226C	08:21:01.568572	16.38	08:21:11.168562	2.43	4.6	4.7	7.7	38.0
210720I	18:01:02.032114	18.24	18:01:08.496112	5.44	2.4	267.9	-55.5	26.7	211226D[•]	08:22:08.048565	27.14	08:22:16.432562	4.74	2.8	251.0	63.7	43.8
210723A	00:25:58.593597	23.94	00:26:06.529584	6.40	3.3	62.2	-37.4	63.1	211226E[•]	19:44:24.609138	19.84	19:44:32.033124	6.34	2.8	264.4	19.6	22.6
210723D[•]	09:24:40.000650	36.80	09:24:59.200650	12.10	3.2	136.6	24.2	32.0	220108F	22:02:34.592243	23.55	22:02:36.704234	22.40	4.1	203.0	-23.2	56.7
210723F	17:07:56.555962	65.15	17:08:14.987962	5.57	2.6	197.6	-2.2	84.2	220109A	09:59:09.504625	20.10	09:59:18.144614	6.85	3.5	18.8	-42.2	49.6
210730B	16:43:23.872428	32.70	16:43:48.000424	4.67	4.3	20.6	-11.9	35.4	220118B	07:38:50.593205	23.10	07:38:56.801200	4.10	3.6	178.7	-50.3	11.8
210809B	08:38:08.006731	26.30	08:38:11.590716	11.20	3.2	223.4	24.5	31.3	220118C	07:53:42.945207	29.70	07:53:44.675320	24.83	4.2	90.0	-8.4	16.3
210811C	11:44:10.367797	41.02	11:44:36.095978	9.66	3.1	219.3	-63.8	49.2	220123A	06:39:21.120816	20.42	06:39:25.792806	9.79	2.6	17.7	26.4	76.8
210813A[•]	06:28:27.296887	27.26	06:28:36.384886	25.34	4.1	292.6	-44.9	16.6	220123C	19:56:35.547598	48.26	19:56:43.291596	8.90	3.1	147.1	-52.6	32.7
210820D	19:42:03.505921	36.22	19:42:13.489912	17.34	4.1	30.1	-27.3	13.3	220125B	09:57:34.592371	16.13	09:57:44.063362	3.52	2.9	128.6	-3.4	55.8
210821D	15:50:47.841371	25.66	15:50:50.273366	17.47	4.6	36.4	74.1	33.2	220126A[•]	11:10:50.000618	27.65	11:11:06.768618	14.40	3.2	261.1	18.0	18.5
210904B[•]	06:20:35.696738	22.72	06:20:45.424724	11.39	4.0	347.9	-5.7	79.9	220128B	07:56:19.408297	30.53	07:56:29.968282	11.52	4.1	27.1	-40.3	29.6
210910C	17:16:30.416798	32.64	17:16:53.776788	1.22	3.6	92.4	69.1	75.3	220217E[†]	14:05:39.648101	21.38	14:05:53.856098	1.47	4.7	263.8	60.9	25.9
210914B	12:42:57.029762	29.50	12:43:07.269762	11.52	3.9	233.4	-51.9	80.0	220224A	01:09:36.118348	25.28	01:09:40.726338	11.14	2.9	259.9	-8.3	68.5
211005D	06:37:18.329975	28.93	06:37:22.233974	31.81	2.7	38.0	-2.8	22.2	220328D	21:34:14.160096	26.05	21:34:10.256082	25.47	4.3	88.2	-57.2	33.8
211031B	13:14:02.272344	15.55	13:14:09.952340	4.03	4.1	302.1	-12.1	29.5	220426B	13:15:32.332059	43.39	13:15:36.748050	24.13	2.2	103.3	-73.9	9.2
211116E[•]	11:19:40.144135	22.08	11:19:48.720130	5.63	4.3	132.4	0.6	22.2	220604A[•]	06:46:05.536726	15.81	06:46:14.176722	3.52	4.3	296.2	-9.8	78.2
211120B	02:10:58.240820	17.41	02:11:08.416810	3.90	4.3	179.1	-31.6	52.0	220609C	11:22:03.377516	19.01	11:22:07.793514	11.90	4.1	111.4	18.3	3.5

Note—We use the localization error as the equivalent radius of the error region, see column 'err'.

†The event is considered to be a likely spark event after manual inspection.

*The event is part of a long burst.

•The event is located in the earth occlusion region.

④ According to the location, the signal of the event come from the sun.

Table 10. Candidates without significant burst signal of unknown events.

Can.ID	Start of $T_{90,F}$ (UTC)	$T_{90,F}$ (s)									
210702B	13:40:13.6333995	35.90	211005E	07:06:08.320430	21.44	220112B	12:23:07.248419	24.58	220414B	03:44:13.700404	21.12
210703A	00:22:14.944398	19.26	211005F	07:14:45.808425	53.50	220112C	13:15:45.392294	34.69	220414C	04:13:16.673906	34.82
210703C	02:53:57.376001	28.54	211005G	08:34:32.497621	57.15	220112D	13:20:54.208282	37.70	220414D	12:46:42.080356	29.82
210703D	03:14:50.528868	29.57	211006A	04:24:54.292826	32.77	220112E	13:21:46.816282	13.12	220415A	01:57:08.706212	39.23
210703E	04:48:31.556519	22.27	211006B	06:10:06.523777	28.10	220112G	15:52:03.569711	30.40	220415B	04:39:53.377163	18.37
210703G	06:38:56.937562	25.34	211006C	08:07:20.416088	25.86	220113A	00:45:24.454114	30.72	220415C	04:43:26.849162	23.81
210703H	08:36:49.824151	19.65	211006D	09:45:22.871300	37.12	220113B	03:39:21.612292	31.42	220415D	07:39:42.691070	15.81
210703I	13:31:50.032010	22.21	211006E	12:00:50.000454	36.42	220113C	03:41:29.212295	16.70	220415E	10:09:48.448022	15.23
210703J	14:34:26.736410	83.20	211007A	01:05:36.240931	53.70	220113D	05:43:25.696196	34.24	220415F	11:03:30.000058	23.10
210704A	04:48:17.502145	19.33	211008A	00:44:26.594404	18.30	220113E	06:18:57.264014	36.67	220415G	11:28:02.496065	23.42
210704B	07:49:48.500648	20.61	211008B	04:08:25.937463	17.66	220113F	13:40:00.801782	19.14	220415H	12:30:37.616462	32.32
210704C	08:42:18.416037	24.90	211008C	18:08:10.001880	20.54	220114A	01:24:18.000000	39.36	220415I	12:51:10.000448	7.36
210706A	07:13:19.188994	23.87	211008D	23:20:49.44154	44.99	220114B	01:37:43.552727	77.95	220415J	12:58:27.327466	14.46
210706B	18:20:02.033324	16.19	211009A	03:01:40.000662	38.34	220114C	05:24:23.008723	26.82	220415M	20:41:10.250538	96.19
210707A	01:53:52.437532	40.64	211010A	03:02:58.915145	31.17	220115A	01:10:37.299566	35.39	220416A	00:53:28.643013	40.19
210707B	07:17:20.001496	38.78	211010B	16:13:40.000628	19.97	220115B	03:20:26.689754	43.65	220416B	00:59:32.543807	27.39
210707C	10:57:55.613827	36.10	211011A	06:06:13.440291	66.50	220115C	05:19:28.210351	32.58	220416C	01:58:36.224072	19.78
210707D	11:19:32.784350	31.23	211011B	08:46:09.553313	40.38	220115D	14:48:52.240072	37.70	220416D	03:45:13.949116	21.82
210707E	17:25:49.569115	50.37	211011C	13:51:22.657946	25.09	220115E	18:21:15.568006	82.37	220416E	05:07:52.816043	27.52
210708A	07:01:54.064412	46.46	211012A	01:25:24.205522	47.81	220115F	21:52:08.570276	11.84	220416F	09:29:57.488050	23.62
210708B	16:54:31.360405	40.38	211012B	03:43:08.506054	29.57	220116A	00:36:09.792455	30.14	220416G	09:50:26.304053	40.00
210709A	03:15:41.258937	18.94	211012C	03:54:22.778057	40.32	220116B	02:15:42.768862	33.60	220416H	11:30:31.024207	38.91
210709B	09:01:24.945984	33.41	211012D	07:01:57.137013	30.59	220116C	07:55:10.803099	25.02	220416I	16:34:48.384911	26.37
210709C	12:36:42.912818	23.04	211013E	18:44:46.093814	28.61	220116D	07:58:42.689137	25.15	220416J	23:47:01.806812	36.22
210709D	16:57:20.351379	29.38	211013A	00:14:56.481549	23.62	220116E	07:59:32.863821	27.07	220417B	11:35:23.520151	16.45
210710A	02:50:45.816408	34.69	211013B	04:44:33.146783	37.25	220116F	08:03:50.481133	30.59	220417C	13:13:07.968519	19.52
210710B	03:25:02.401024	25.02	211013C	21:09:28.872016	24.06	220116G	18:07:52.370437	57.98	220417E	22:35:59.488929	40.45
210710C	07:30:52.392014	36.54	211014A	03:38:20.945518	33.60	220117A	00:10:27.041608	32.90	220417F	22:36:30.000916	63.81
210711B	08:07:40.256403	25.54	211014B	06:32:00.000404	33.28	220117B	00:43:47.480002	32.38	220417G	23:46:48.078553	22.21
210711C	14:57:47.231566	19.52	211015A	01:02:18.321939	31.62	220118A	00:57:59.998576	43.01	220418A	03:21:20.128475	39.81
210712A	23:49:38.736379	26.75	211015B	01:25:46.177935	27.20	220118D	11:59:02.594396	39.36	220418C	16:40:45.376011	50.56
210713A	06:04:38.064959	31.74	211015C	04:55:03.766558	28.54	220118F	22:58:17.511366	20.93	220418D	17:23:47.057889	2.88

Table 10 *continued on next page*

Table 10 (continued)

Can.ID	Start of $T_{90,F}$ (UTC)	$T_{90,F}$ (s)									
210713B	09:40:32.256626	27.26	211015D	21:43:10.385781	20.61	220119A	07:46:58.400389	27.14	220418E	20:18:14.430693	25.28
210713C	13:41:24.480014	35.46	211015E	23:13:18.320302	31.62	220119B	09:43:37.280360	22.66	220418F	21:57:59.999208	31.04
210713E	23:06:35.490179	21.25	211016A	00:37:08.512045	32.77	220120A	05:58:02.879994	45.38	220418G	23:58:00.000276	32.38
210715A	00:28:18.305007	33.54	211016B	04:10:53.504447	24.32	220120B	06:01:46.848005	35.46	220419A	00:10:07.904287	34.18
210715B	07:27:07.120128	33.98	211016C	21:23:05.296129	31.81	220120C	08:27:41.953522	34.82	220419B	02:15:19.793236	15.10
210715C	22:20:20.044410	29.06	211017A	00:55:54.104231	38.53	220120D	19:39:08.128526	35.39	220419C	03:04:15.376235	29.95
210716A	00:07:32.448692	28.80	211017B	02:54:00.000216	32.90	220120E	20:33:35.088019	6.85	220419D	03:34:18.576243	31.36
210716B	00:32:20.352683	20.86	211017C	22:25:35.476036	77.63	220120F	20:44:50.842888	20.22	220419E	10:39:48.832607	31.10
210716C	04:32:13.040014	32.90	211017D	22:57:32.446751	24.96	220120G	21:15:10.256291	32.83	220419F	18:38:58.058024	27.33
210716D	18:44:44.275584	28.22	211017E	23:24:05.201356	26.94	220120H	22:33:40.799365	32.19	220419G	20:30:04.592373	29.38
210716E	19:29:19.906180	21.12	211018A	02:46:53.696022	44.54	220121A	00:17:14.209403	25.15	220419H	20:48:42.512376	47.42
210717A	04:19:35.120140	34.82	211018B	09:00:12.064580	18.11	220121B	02:42:08.832347	18.56	220419I	20:49:20.000364	50.88
210717B	04:56:59.999888	24.83	211019A	01:06:39.360767	31.04	220121D	09:05:41.058953	18.50	220419J	21:56:36.550270	21.44
210717C	18:33:19.034252	39.42	211019B	10:30:49.617466	21.95	220121E	09:50:45.826964	21.76	220419K	22:06:46.528450	17.02
210717D	23:26:39.279940	29.44	211019C	20:21:44.685128	41.66	220121F	21:58:00.000302	58.37	220420A	08:48:33.360328	56.58
210718B	09:09:38.128904	31.81	211020A	00:09:28.720027	22.46	220121G	23:53:21.386455	24.70	220420B	09:58:11.582676	33.79
210718C	09:57:30.160906	19.78	211020B	10:14:31.904644	28.03	220122A	00:25:56.048206	17.54	220420C	12:50:18.048429	38.46
210718D	20:23:24.816158	20.99	211021A	01:09:18.794998	49.66	220122B	02:12:10.704035	21.89	220420D	19:33:53.784774	20.67
210719A	06:05:32.272418	29.76	211021B	09:21:13.121300	23.23	220122C	03:03:58.160683	25.09	220420E	22:24:10.656729	23.55
210719B	12:41:04.504017	18.43	211021C	18:38:41.463198	30.98	220123B	15:59:03.104134	20.80	220421A	07:44:51.888638	24.96
210720C	03:33:10.081450	24.64	211021D	19:52:58.644736	61.25	220124A	10:58:14.744014	32.19	220421B	20:58:00.000050	23.10
210720D	06:24:06.928341	43.01	211021E	20:28:30.496846	33.34	220124B	19:52:27.428503	29.38	220422A	00:47:59.593533	35.71
210720E	11:07:18.625418	33.86	211021F	21:29:55.669520	30.59	220124C	22:58:41.663733	19.14	220422B	01:52:15.000000	25.15
210720F	12:16:34.017798	22.85	211022A	09:18:44.545138	28.03	220125C	14:59:24.737190	16.38	220422C	04:40:22.352506	25.92
210720H	16:08:40.300786	21.50	211022B	16:31:15.058673	32.51	220126B	16:03:30.000136	26.88	220422D	13:25:45.686039	104.26
210720J	18:34:21.360117	28.22	211022C	18:11:50.000016	22.40	220126C	16:30:18.992447	30.40	220422E	17:25:24.000000	15.42
210720K	18:52:32.016116	31.36	211022D	21:18:19.900018	24.70	220126D	21:34:57.600537	33.22	220422F	21:22:21.040189	25.60
210720L	19:50:17.819227	41.60	211022E	21:49:35.276019	32.96	220127A	00:35:10.017663	32.51	220423A	11:28:37.699319	42.24
210721A	01:16:56.224028	30.53	211022F	23:48:20.224812	19.71	220127B	02:46:43.744316	26.56	220423B	18:10:12.832304	28.42
210721B	02:34:06.832015	26.43	211023A	08:40:49.344137	30.59	220127C	08:44:42.289323	37.57	220423C	20:29:36.052174	33.28
210721C	19:18:01.166273	28.10	211023B	18:22:17.888463	24.96	220127D	14:43:34.432336	19.78	220423D	20:33:16.052174	46.08
210721D	21:49:04.433174	27.52	211023C	21:12:09.093982	25.86	220128A	03:02:28.640410	45.06	220424A	18:38:40.722238	27.26
210721E	23:05:35.216883	42.43	211024A	10:31:26.592016	25.34	220128C	10:56:06.668934	23.04	220424B	20:25:06.543393	24.70
210722A	19:04:04.157218	32.19	211024B	14:15:10.597616	26.56	220128D	15:27:07.185502	36.22	220424C	21:04:08.337156	29.31

Table 10 continued on next page

Table 10 (*continued*)

Can.ID	Start of $T_{90,F}$ (UTC)	$T_{90,F}$ (s)	Can.ID	Start of $T_{90,F}$ (UTC)	$T_{90,F}$ (s)	Can.ID	Start of $T_{90,F}$ (UTC)	$T_{90,F}$ (s)	Can.ID	Start of $T_{90,F}$ (UTC)	$T_{90,F}$ (s)
210722B	19:05:41.933216	45.50	211024C	16:24:54.144174	23.23	220128E	19:43:08.224213	24.45	220424D	21:58:20.545151	30.85
210722C	19:13:27.533220	29.95	211024D	21:17:54.432580	24.19	220129A	01:37:37.584443	52.35	220424E	22:07:41.809153	28.61
210723B	00:32:00.001584	46.08	211025A	04:57:11.408205	38.53	220129B	05:29:10.000834	37.18	220425B	11:10:50.000994	30.14
210723C	06:13:53.504660	20.61	211026A	00:29:37.313709	27.14	220129C	17:22:04.784218	34.30	220425C	16:47:44.187014	36.99
210723E	15:28:41.180916	33.41	211026B	18:49:49.346447	30.02	220130A	16:40:52.499757	40.64	220425D	17:11:10.737363	48.96
210723G	18:56:59.999284	27.14	211026C	19:08:55.697031	51.01	220130B	16:44:33.971757	26.62	220425E	19:06:06.528538	35.07
210723H	19:17:54.304318	23.42	211026D	20:38:38.529128	35.90	220130C	17:09:35.520040	28.93	220425F	21:58:23.958301	27.97
210723I	20:25:38.578838	23.62	211026E	22:20:07.179613	16.70	220130D	23:16:20.000690	81.92	220426A	10:50:18.816892	16.70
210723J	22:57:30.270261	29.25	211027A	05:03:14.880304	39.55	220131B	15:15:05.777834	23.49	220426C	16:43:22.779715	32.00
210724A	00:41:30.547181	36.99	211027B	06:19:30.674589	32.06	220131C	16:27:12.752278	47.94	220426D	16:54:22.907715	31.49
210724B	05:02:45.696767	21.44	211027C	13:56:28.774373	33.79	220131D	17:07:39.376923	19.20	220426E	18:09:23.000000	28.93
210724C	05:33:33.184781	26.75	211027D	15:57:47.298065	41.60	220201B	14:38:16.463026	30.14	220426F	18:56:36.780545	29.38
210724D	16:54:35.675616	35.20	211027E	18:37:51.625724	23.68	220201C	23:44:44.080485	36.10	220426G	19:58:32.670277	39.36
210724E	18:45:20.882646	31.55	211027F	22:11:32.160227	27.78	220202A	17:38:49.384195	25.73	220427A	16:50:18.734138	32.83
210724F	21:07:38.032335	19.78	211028A	01:55:40.226092	19.71	220203B	11:39:39.168687	27.26	220427B	17:58:00.000416	18.94
210724G	21:50:59.470552	21.06	211028B	18:16:53.481332	49.60	220203C	12:24:57.000000	30.27	220427C	19:34:09.349544	36.29
210725A	00:28:02.928035	27.01	211028C	18:23:15.833341	38.46	220203D	17:39:47.402891	27.58	220427D	19:35:59.349544	29.18
210725B	09:34:51.203686	19.14	211028D	19:14:05.889240	34.05	220203E	18:37:06.353192	23.36	220429A	01:58:24.256208	36.48
210725C	10:48:06.400824	33.54	211028E	20:26:16.320352	23.62	220203F	23:04:26.192157	27.58	220429C	19:40:09.686155	21.63
210725D	17:12:03.888010	40.26	211028F	20:39:02.608351	27.33	220204A	00:23:01.104242	28.93	220430A	02:11:57.152890	22.78
210727A	00:53:07.217303	27.52	211029A	01:19:33.685072	20.29	220204B	02:06:41.216773	30.78	220430B	05:49:20.720012	49.22
210727B	14:06:20.912014	33.02	211029B	17:58:46.754982	20.54	220204C	14:07:10.000956	29.31	220430C	19:09:16.192981	16.90
210727C	17:01:40.001036	29.38	211029C	18:12:43.257660	36.80	220204D	22:54:26.912512	20.54	220430D	19:49:20.000978	28.61
210727D	18:12:13.232020	30.14	211029D	23:06:20.001046	18.30	220205C	15:17:20.098566	30.02	220430E	19:51:14.352979	52.61
210728A	01:21:55.040021	26.69	211029E	23:46:00.553058	19.14	220205E	17:26:10.961775	57.34	220501B	19:28:47.424836	32.51
210728C	16:18:46.194023	26.56	211030A	12:23:57.624015	29.31	220205F	18:18:41.240015	29.70	220502A	15:47:07.251743	32.26
210728D	22:22:12.448366	47.49	211030B	14:34:15.769442	30.40	220206A	04:15:24.592803	35.58	220502B	16:08:00.754384	52.61
210729A	06:42:34.034190	25.54	211030D	21:38:27.530854	30.91	220206B	06:46:35.864006	83.07	220502C	21:56:37.974168	20.54
210729B	17:33:52.6689500	28.35	211030E	21:45:36.218870	21.25	220206C	10:15:17.057054	24.06	220502D	22:12:50.369526	23.10
210730A	14:11:16.801015	25.54	211031A	10:28:40.000359	39.94	220206D	10:59:33.764879	26.18	220502E	22:15:03.281529	28.80
210731A	12:04:49.742854	27.90	211031C	14:44:37.292501	32.51	220206E	11:47:44.284108	36.67	220503A	04:36:12.032009	33.66
210731B	15:41:44.432802	41.79	211031D	14:58:10.655546	49.28	220206F	14:11:37.040830	20.35	220503B	13:25:07.542886	33.28
210731C	19:11:50.000152	52.86	211101B	12:43:39.741852	27.90	220206G	16:06:20.288606	32.13	220503C	13:26:40.262883	50.56
210801A	13:51:17.199821	51.20	211101C	16:07:19.456256	37.76	220206H	23:29:37.968919	18.50	220503D	13:27:40.470875	100.35

Table 10 *continued on next page*

Table 10 (*continued*)

Can.ID	Start of $T_{90,F}$ (UTC)	$T_{90,F}$ (s)	Can.ID (UTC)	Start of $T_{90,F}$ (UTC)	$T_{90,F}$ (s)	Can.ID (UTC)	Start of $T_{90,F}$ (UTC)	$T_{90,F}$ (s)	Can.ID (UTC)	Start of $T_{90,F}$ (UTC)	$T_{90,F}$
210801B	16:13:53.664896	24.19	211101D	19:10:55.220711	16.00	220207A	06:34:54.160119	86.98	220503E	20:51:38.544039	31.04
210801C	19:21:03.168320	33.73	211102A	15:43:44.770451	46.53	220208A	06:19:49.824006	82.11	220503F	22:15:43.088546	46.85
210802A	03:08:25.488611	30.08	211103A	13:47:53.010101	26.24	220208B	11:16:50.803370	47.94	220504A	13:27:24.167775	53.76
210802B	07:32:07.488537	18.30	211103B	14:46:57.792041	31.74	220208C	12:12:53.696858	19.33	220504B	15:05:39.712115	24.83
210802C	12:01:00.304370	29.25	211105A	10:01:20.145721	33.28	220208D	21:39:35.328764	17.34	220505A	11:58:46.145372	31.94
210802D	14:55:58.700076	56.83	211105B	13:40:27.199169	20.67	220209A	04:27:32.929083	86.98	220505B	14:31:10.463234	63.30
210802E	15:35:08.464165	29.12	211105C	13:56:05.487161	40.64	220209B	06:06:21.688006	85.25	220505C	14:51:41.583237	28.03
210802F	16:42:27.090594	35.52	211105D	13:58:57.282159	20.61	220209C	06:46:41.317021	18.62	220505D	17:02:45.536251	29.50
210802G	21:57:04.049136	45.89	211105E	20:50:28.384011	28.61	220209D	11:27:28.626272	39.81	220505E	17:57:45.490498	40.13
210802H	22:56:00.235618	37.50	211106B	14:41:18.821096	34.24	220209E	12:42:02.000000	17.41	220506A	13:06:14.976213	31.23
210803A	13:03:45.194312	54.02	211107A	09:57:11.925776	45.18	220209F	14:22:27.091126	41.09	220506B	15:52:21.046694	41.28
210803B	13:53:15.194312	24.70	211107B	16:46:07.080506	23.17	220209G	19:42:11.328176	21.25	220507A	00:52:28.209171	41.73
210804A	03:42:29.104839	27.14	211107C	18:36:28.286140	22.14	220209H	20:11:51.760768	29.25	220507B	01:35:01.634430	31.68
210804B	11:22:24.771274	59.71	211107D	19:30:10.000320	43.14	220210A	06:25:42.225178	23.30	220507C	15:49:50.173456	31.10
210804C	14:27:43.153034	38.27	211108A	10:52:02.182252	31.04	220210B	08:42:32.963861	25.66	220508B	13:44:05.000000	49.92
210804D	14:31:12.65732	23.62	211108B	22:18:15.424495	28.35	220210C	12:43:14.077392	25.47	220508C	14:30:29.040627	40.90
210804E	20:13:17.680406	22.08	211109B	06:03:06.944358	32.45	220210D	12:47:43.997601	32.90	220508D	15:22:46.000000	27.90
210804F	22:44:50.000358	28.35	211109C	10:51:37.786133	28.67	220211A	01:32:14.048062	45.89	220509A	04:44:08.051407	25.54
210805A	16:54:34.176760	39.10	211109D	12:28:59.000000	55.94	220211B	04:00:56.481211	90.75	220509B	06:05:55.136142	34.11
210805B	17:40:19.053188	21.25	211109E	16:29:36.544387	24.51	220211C	05:39:22.808000	34.30	220509C	10:50:57.604989	32.45
210805C	20:45:28.657196	24.13	211110A	10:26:51.891004	48.77	220211D	05:38:51.000000	21.06	220509D	12:41:18.352279	41.28
210805D	22:20:40.624501	29.31	211110B	15:42:13.470218	20.29	220211E	09:35:19.104158	26.69	220509E	13:47:13.663472	19.90
210805E	23:03:59.040953	28.86	211110C	17:17:34.272088	46.91	220211F	14:41:31.344267	38.59	220509F	15:12:49.993757	31.62
210806A	14:46:21.193606	22.78	211110D	18:51:40.832131	39.10	220211G	21:52:52.849121	17.09	220510B	10:15:02.800768	25.34
210806B	15:02:42.976584	28.22	211111A	10:11:32.639238	32.38	220212B	14:24:59.297477	31.49	220510C	10:30:11.408773	43.78
210806C	23:11:50.000302	35.33	211111B	19:57:11.857289	28.35	220213A	10:08:41.000000	38.91	220510D	20:04:12.308549	29.44
210807A	10:31:27.388691	27.78	211111C	20:34:33.969047	22.98	220213B	10:13:20.447383	32.58	220511A	12:38:30.113090	30.46
210807B	10:58:30.751335	29.18	211112A	10:10:52.992011	30.85	220213C	12:25:46.128417	17.28	220511B	13:30:43.147287	19.14
210807C	14:01:41.584175	25.41	211112B	10:54:46.272010	42.18	220213D	12:58:26.752754	36.03	220512C	10:28:05.952576	36.22
210807E	23:38:45.776846	44.16	211112C	11:56:33.934100	26.30	220213E	22:36:31.728080	29.38	220512D	11:16:54.274124	40.00
210808A	08:08:12.552016	24.38	211112D	12:30:42.832069	22.46	220214A	00:47:03.072876	36.86	220513A	06:04:09.728714	17.54
210808B	10:29:31.605282	25.09	211112E	21:14:53.344928	26.56	220214B	03:19:20.392007	76.54	220513B	07:49:29.387376	44.61
210808C	10:43:12.101290	35.46	211113A	03:08:08.806959	88.90	220214C	08:16:15.000000	41.15	220513C	07:50:40.603370	35.46
210808D	12:14:41.697376	32.83	211113B	04:54:47.875390	23.23	220214D	21:26:15.505701	32.06	220513D	09:37:28.319943	33.60

Table 10 *continued on next page*

Table 10 (*continued*)

Can.ID	Start of $T_{90,F}$ (UTC)	$T_{90,F}$ (s)									
210808E	12:22:51.025366	28.74	211113C	10:19:38.545361	17.47	220215A	01:25:20.808007	80.13	220513E	10:55:47.000000	78.46
210809A	08:23:44.374716	28.74	211113E	15:11:08.544107	31.62	220215B	03:05:37.560004	93.38	220513F	13:04:46.992145	28.42
210809C	10:25:36.584513	26.30	211113F	15:16:49.424109	19.71	220215C	05:31:13.760162	40.96	220514A	05:50:10.701392	25.22
210809D	10:39:22.120504	30.66	211114A	06:17:07.601084	45.25	220215D	05:37:50.320173	28.16	220514C	14:44:09.101268	42.75
210809E	11:05:35.808085	21.12	211114B	07:54:00.299554	54.14	220215E	08:20:33.290377	26.24	220515A	02:11:55.208569	74.62
210809F	13:48:30.437871	36.54	211114C	07:57:26.367648	30.85	220216A	06:13:41.025736	19.01	220515B	03:51:38.408005	86.53
210809G	16:12:48.689016	29.95	211114D	08:39:33.888598	41.34	220216B	08:15:02.320397	23.36	220515C	05:30:59.000000	21.63
210809H	17:54:00.000324	33.79	211114E	09:53:11.771364	33.41	220216C	13:54:05.600161	30.72	220515D	07:19:29.064212	15.81
210810A	07:07:11.072080	31.30	211114F	10:16:04.754852	28.03	220216D	16:54:11.104202	28.93	220515F	23:50:11.328958	24.51
210810B	07:35:18.000086	31.94	211114G	13:17:49.952535	45.89	220217A	04:25:44.787322	21.31	220516A	10:33:00.211299	19.26
210810C	09:49:15.396498	41.22	211115A	00:08:40.176645	29.76	220217B	04:37:32.067312	34.56	220516B	17:43:10.592994	23.62
210810D	15:08:10.001734	63.17	211115B	08:00:50.000270	37.70	220217C	08:04:19.344620	23.10	220517A	08:30:20.071216	30.72
210811A	11:14:42.047978	43.01	211115C	13:49:46.288512	18.62	220217D	12:17:53.954901	25.98	220517B	17:25:04.161726	20.80
210811B	11:20:43.919983	40.32	211115D	16:15:30.000916	35.90	220218B	07:23:19.681240	29.95	220517C	17:51:26.897715	43.39
210811D	14:39:49.027800	33.60	211116A	02:28:22.131329	87.30	220218C	07:49:13.761242	19.26	220517D	20:46:08.545309	24.32
210811E	22:55:50.000392	24.58	211116B	04:14:47.190124	21.44	220218D	09:18:24.721860	21.89	220518A	08:07:21.000000	64.70
210812A	12:01:22.928133	27.01	211116C	08:01:20.016147	27.65	220218E	19:35:34.531191	29.82	220518B	13:13:52.428346	26.18
210812B	16:53:33.136352	36.80	211116D	08:40:37.376155	42.56	220219A	10:39:46.669381	36.22	220518C	13:27:07.708350	24.58
210813B	09:09:04.401168	56.64	211116F	18:02:56.513443	36.22	220220A	00:18:37.536007	78.40	220519A	08:58:39.935632	22.02
210813C	20:33:28.832313	31.10	211116G	18:05:42.129452	20.99	220220B	02:30:50.224112	19.71	220519B	11:12:03.778142	27.71
210814A	07:29:48.577589	23.81	211116H	22:52:16.062264	56.96	220220C	04:06:09.920938	29.89	220520A	07:45:29.783193	80.13
210814B	08:22:41.776724	30.14	211116I	22:53:23.134264	15.17	220220D	05:58:16.576415	26.56	220520B	07:47:01.799190	98.11
210814C	09:13:40.000182	32.13	211117A	06:33:06.688587	38.27	220220E	06:13:25.440419	32.38	220520C	07:48:29.975186	39.17
210816A	05:12:59.932494	19.84	211117B	06:43:58.688586	17.41	220220F	22:26:17.648217	90.69	220520D	10:57:47.629326	7.81
210816B	10:38:44.749956	28.42	211117D	09:26:53.489232	35.39	220221A	00:05:02.536005	86.40	220520E	13:58:22.656696	25.66
210816C	13:12:04.528902	26.69	211117E	15:19:40.976099	24.64	220221B	05:02:00.856002	36.22	220521A	06:23:17.040590	32.90
210817A	03:18:44.186204	25.02	211119A	13:01:44.464399	30.78	220221C	05:13:05.596753	27.71	220521B	09:11:42.583379	16.38
210817B	06:53:46.573004	28.80	211120A	01:38:12.273024	28.93	220221D	22:11:35.176007	77.76	220521C	12:08:01.712160	19.46
210818A	08:37:02.017190	28.42	211120C	03:30:41.917999	40.38	220221E	23:51:36.544006	83.39	220522A	01:44:59.633103	40.13
210818B	12:43:52.352031	23.62	211120D	05:19:10.001282	32.70	220222A	00:10:02.849226	57.09	220522B	12:24:05.984034	25.60
210818C	16:09:36.784422	33.15	211121A	01:54:06.677376	21.57	220222B	01:43:29.648186	40.77	220522C	12:57:21.408037	31.68
210818D	19:57:29.695639	21.44	211121B	03:08:27.052202	24.51	220222C	06:39:53.112246	32.26	220522D	16:41:20.080019	29.44
210819A	02:12:07.569247	20.93	211121C	03:11:04.396192	31.17	220222D	09:16:20.000952	23.42	220523E	17:58:54.337697	20.54
210819B	03:01:12.593448	42.62	211121D	03:27:34.396192	25.41	220222E	09:18:10.000952	20.99	220523A	05:58:08.071889	31.04

Table 10 *continued on next page*

Table 10 (*continued*)

Can.ID	Start of $T_{90,F}$ (UTC)	$T_{90,F}$ (s)	Can.ID (UTC)	Start of $T_{90,F}$ (UTC)	$T_{90,F}$ (s)	Can.ID (UTC)	Start of $T_{90,F}$ (UTC)	$T_{90,F}$ (s)	Can.ID (UTC)	Start of $T_{90,F}$ (UTC)	$T_{90,F}$ (s)
210819C	03:13:40.001444	31.10	211121E	05:17:50.336175	21.50	220222F	21:58:09.952006	81.98	220523B	07:58:44.672043	24.45
210819D	04:53:38.630462	40.90	211121F	08:38:44.369074	28.74	220223A	06:47:09.281728	33.79	220524A	02:42:50.752052	32.13
210819E	09:48:43.042752	34.11	211121G	15:20:13.232764	23.87	220223B	21:44:50.424006	80.51	220524B	03:29:35.331540	24.13
210819F	14:08:58.256214	41.28	211121H	23:36:10.807483	31.55	220224B	02:51:18.232286	40.19	220524C	05:39:36.362080	20.61
210819G	16:52:39.184501	18.56	211121I	23:53:32.775492	23.23	220224C	04:31:04.064907	54.78	220524D	18:23:40.003910	21.25
210819H	17:57:36.287870	20.74	211122A	05:27:34.064651	37.31	220224D	21:47:16.115787	28.99	220525B	03:13:57.143544	27.46
210820A	02:04:16.976122	26.62	211122B	09:25:21.486016	39.04	220224E	23:15:48.321244	34.05	220525C	03:45:30.183547	25.02
210820B	03:15:46.768641	28.48	211123A	02:50:06.276519	28.80	220224F	23:17:38.321244	26.62	220525D	09:44:41.178902	29.76
210820E	19:43:00.001912	45.50	211123B	14:42:22.576370	23.42	220225A	02:59:16.735223	29.70	220525E	14:24:19.808655	23.74
210821A	02:50:21.719192	30.34	211124A	00:11:39.464014	33.47	220225B	04:11:00.901242	37.06	220526B	09:12:11.793365	19.14
210821B	05:20:55.360012	48.58	211124B	03:32:31.073059	18.94	220226A	01:19:04.976495	25.09	220526C	10:38:30.049906	27.01
210821C	11:08:58.257976	37.70	211124C	04:26:45.744697	30.08	220226B	08:35:16.545184	22.14	220526D	11:54:33.889503	26.05
210821E	18:19:19.217154	36.93	211124D	05:44:00.781592	21.12	220226D	14:08:04.400131	20.54	220526E	20:15:58.576307	17.41
210821F	18:50:02.161167	27.78	211124E	06:29:18.432486	21.89	220226F	16:11:09.329525	20.74	220527A	03:36:43.120964	29.25
210822A	00:32:50.598580	43.07	211124F	12:15:58.416131	17.09	220226G	22:46:52.618119	6.02	220527B	08:26:06.736028	26.69
210822B	02:11:59.657762	31.30	211124G	12:58:36.446902	23.49	220227A	02:12:06.38493	27.71	220527C	21:33:06.456007	76.48
210825A	23:39:31.401114	45.76	211125A	02:13:29.100948	36.67	220227B	05:27:16.676064	24.51	220528A	01:08:29.4241929	40.51
210826A	05:12:12.273260	32.45	211125B	03:20:49.472600	23.94	220228A	06:38:21.626454	34.11	220528B	02:56:16.321849	30.27
210826B	16:24:04.816238	24.83	211125C	04:19:48.528812	33.34	220228B	13:10:34.080491	25.86	220528C	03:00:10.928449	33.86
210827A	00:27:52.560709	29.70	211126A	03:37:50.244748	42.37	220228C	14:50:48.323332	31.62	220528D	11:20:22.080124	22.14
210827B	02:10:16.354692	43.58	211126B	04:17:23.392167	19.78	220228D	23:24:53.920416	33.92	220528E	15:43:50.001464	38.02
210827C	03:18:10.304326	25.79	211126C	06:11:19.312609	47.10	220301B	22:04:12.202906	29.12	220528F	18:28:26.048051	20.86
210827D	12:33:24.032202	35.90	211126D	12:37:04.736332	19.65	220302A	02:04:02.769375	31.55	220528G	23:56:50.341564	27.90
210827E	13:22:50.000526	31.04	211128A	14:58:18.975695	25.60	220302B	03:48:14.808098	35.07	220529A	04:55:37.616176	37.89
210827F	17:15:05.120048	34.82	211128B	17:20:31.664305	38.27	220302C	03:59:08.160309	27.58	220529B	09:53:00.002198	45.06
210827G	20:08:32.464328	36.74	211128C	21:25:01.432014	37.50	220303A	01:26:02.081299	22.78	220529D	13:37:36.560213	44.10
210827H	22:31:28.465067	21.70	211129A	21:11:56.720016	25.22	220303B	14:06:36.800239	27.78	220530A	06:08:18.609969	36.99
210827I	23:37:49.291384	49.92	211130A	01:08:44.240296	35.07	220304A	08:38:48.480447	21.70	220531A	03:07:22.136016	20.80
210828A	02:01:41.345334	28.10	211130B	01:24:16.976304	32.96	220304B	11:30:49.777024	20.16	220531B	07:52:39.792075	30.14
210828B	04:16:58.364680	19.33	211130C	02:10:02.528164	33.47	220304C	18:54:34.112395	29.89	220531C	09:24:00.098189	20.99
210828C	06:03:16.896898	23.04	211130D	04:37:01.797837	36.74	220304D	19:14:11.688016	21.25	220531D	13:10:17.760699	42.18
210828D	06:06:10.752890	69.18	211130G	20:00:50.000436	24.00	220304E	20:40:45.928005	30.98	220531E	21:12:40.002086	25.15
210828E	06:10:14.880894	45.06	211201A	23:34:51.052098	37.57	220305A	15:03:07.488538	29.12	220601A	00:19:17.330147	23.68
210828F	06:11:34.224889	20.54	211201A	01:03:50.848128	30.72	220305B	19:58:43.968411	42.37	220601B	01:53:52.402892	18.24

Table 10 *continued on next page*

Table 10 (*continued*)

Can.ID	Start of $T_{90,F}$ (UTC)	$T_{90,F}$ (s)									
210829A	00:51:04.684958	40.77	211201B	02:29:28.611262	31.30	220305C	22:24:37.464014	33.47	220601C	02:11:35.696352	34.43
210829B	04:09:38.960609	30.98	211201C	10:00:50.000334	22.27	220305D	23:19:30.896723	39.04	220601D	09:57:06.560094	44.54
210829C	05:12:25.040220	24.90	211201D	19:48:17.957369	20.10	220306A	00:05:41.552013	40.38	220601G	15:30:24.496580	45.44
210829D	10:10:13.952570	28.48	211201E	21:42:26.020050	17.41	220306C	18:22:01.969842	19.26	220601H	22:27:56.207522	20.42
210829E	12:05:59.408901	30.53	211201F	21:49:47.236050	45.89	220306D	22:34:43.624242	31.87	220602A	00:08:46.512802	23.42
210830A	02:38:55.237397	19.52	211201G	22:56:59.999086	39.17	220307A	06:34:53.441598	21.95	220602B	01:45:48.737946	33.60
210830B	09:05:36.945181	37.44	211201H	23:08:35.216622	26.50	220307B	08:29:11.536078	35.26	220602C	02:26:55.824226	24.19
210830D	13:26:12.288857	27.65	211202A	00:41:24.731391	33.41	220307C	09:20:26.112500	35.97	220602D	03:41:00.425704	28.10
210830F	18:30:28.496545	17.47	211202B	21:24:34.486631	41.28	220307D	20:03:38.576595	34.18	220602E	03:44:50.345706	30.46
210830G	20:24:23.960013	38.98	211203A	19:33:56.561818	46.78	220307E	20:48:28.379403	16.90	220602F	08:11:44.720315	30.40
210831A	02:03:10.336201	43.20	211203B	22:33:06.081804	34.75	220307F	20:53:16.331396	57.54	220603A	00:07:34.129054	22.02
210831B	04:00:18.608445	25.66	211204B	03:43:13.494227	29.18	220307G	20:58:32.395412	23.87	220603B	02:17:46.528168	21.50
210831C	14:17:21.280808	24.58	211204C	22:19:33.226948	63.62	220308A	00:32:03.809361	34.05	220603C	08:21:03.040518	20.86
210831D	19:15:38.113726	26.24	211205A	02:53:34.976016	24.96	220308B	01:43:03.195957	29.44	220603D	12:34:20.688533	29.25
210831E	20:11:30.808016	24.13	211205B	08:07:34.852398	39.62	220308C	10:43:20.449063	22.08	220603E	14:12:05.328344	44.61
210831F	20:42:05.873656	27.20	211205C	19:08:10.000164	30.08	220308D	19:18:20.112922	21.76	220603F	20:02:28.448746	32.96
210831G	22:30:11.924054	24.26	211205D	19:18:42.496178	24.45	220308E	21:24:19.617723	33.79	220603G	21:38:12.095276	34.82
210901A	02:01:32.880009	23.04	211205E	22:16:35.025447	35.07	220308F	23:46:03.045288	27.07	220603H	21:42:10.655279	21.38
210901B	08:22:50.000314	26.30	211205G	22:47:15.521442	54.14	220309A	02:57:46.752355	31.17	220603I	23:56:56.758624	28.22
210901C	17:34:29.806809	30.78	211206A	02:21:25.689818	15.68	220309C	12:28:25.920071	21.44	220604B	08:14:01.217131	38.72
210901D	22:51:36.726518	40.13	211206B	18:46:22.681887	24.32	220309D	21:07:40.593759	22.85	220604C	14:47:16.039675	20.16
210901E	23:02:52.064584	28.48	211206C	19:17:39.777027	17.60	220309F	23:58:00.000342	47.04	220604D	21:53:00.425900	20.10
210901F	23:20:00.000572	25.09	211206D	20:22:30.030040	35.39	220310B	20:03:01.993454	55.62	220605A	00:17:30.464174	29.31
210902A	06:08:29.968217	21.57	211206E	22:54:55.040723	31.36	220310C	20:28:41.993454	24.90	220605B	13:32:08.416515	37.82
210902B	18:44:19.450508	29.06	211207A	20:27:29.904238	22.21	220311A	09:13:04.065526	19.90	220605C	17:51:50.384170	24.64
210902C	23:44:24.371353	14.53	211207C	22:19:41.617177	25.22	220311B	09:44:30.641529	50.69	220605D	22:23:01.896013	39.04
210903A	00:21:55.936667	21.38	211207D	23:20:10.770206	27.33	220311C	15:59:18.144029	30.46	220606A	03:56:30.354178	26.43
210903B	04:44:59.665610	26.50	211208A	04:42:17.968693	29.76	220311D	16:42:32.564336	35.39	220606B	11:49:07.152108	22.78
210903C	06:55:24.160532	35.78	211208B	09:01:32.624305	28.99	220311E	18:17:20.525395	18.37	220606D	18:05:46.432820	30.85
210903D	07:44:50.000370	24.45	211208C	13:54:13.780845	19.52	220311G	19:23:54.088016	22.85	220606E	22:33:13.278320	23.74
210903E	18:28:29.490242	37.31	211208E	18:10:27.280257	32.19	220312A	04:55:56.048721	16.06	220607A	00:22:56.057874	37.31
210903F	20:00:02.881370	35.58	211208F	21:48:47.697423	37.57	220312B	19:02:45.152309	20.86	220607B	00:41:16.057874	22.59
210904A	03:23:44.400963	21.70	211209A	07:07:46.785522	33.15	220312C	21:14:21.042496	37.06	220607C	02:08:00.944038	40.13
210905A	09:46:08.081033	29.95	211209B	14:43:10.185076	42.88	220313A	02:59:31.391777	28.54	220607D	13:17:36.544667	43.39

Table 10 *continued on next page*

Table 10 (continued)

Can.ID	Start of $T_{90,F}$ (UTC)	$T_{90,F}$ (s)									
210905B	13:37:57.904457	39.55	211209C	20:07:43.200350	36.74	220313C	08:57:35.872789	30.08	220607E	15:41:07.902552	72.19
210905C	19:35:32.792045	23.23	211209D	23:48:57.584159	66.24	220313D	17:59:23.520028	15.74	220607F	19:22:34.288073	28.61
210906A	01:06:34.753136	27.20	211210A	00:05:39.568015	26.37	220313E	19:40:31.788693	30.08	220607G	21:56:21.712433	28.22
210906B	02:23:25.265642	38.85	211210B	00:50:18.095883	30.91	220313F	20:17:30.849332	35.78	220608A	17:14:19.585814	19.58
210906C	16:15:27.595772	36.61	211210C	02:20:24.688934	20.99	220313G	21:03:30.000308	35.46	220608B	19:58:25.727326	23.30
210907A	03:28:49.760055	20.03	211210D	19:21:42.967209	26.75	220314B	01:10:51.872336	8.06	220608C	20:27:42.660622	19.07
210907B	14:48:22.639775	24.38	211211A	05:39:49.632257	17.15	220314E	18:09:49.344116	25.98	220608D	21:37:07.826362	35.26
210907C	18:14:47.585593	36.42	211211B	08:24:51.330426	26.24	220314F	18:44:00.360014	32.58	220608E	21:42:40.896015	31.04
210907D	19:12:40.935121	44.54	211211C	17:56:10.384412	25.54	220315A	00:57:47.456153	19.71	220609A	02:28:29.952261	23.81
210907E	19:27:46.215126	19.01	211211D	22:48:23.413342	17.02	220315C	18:08:06.769481	49.92	220609B	04:42:54.592349	36.74
210907F	20:54:43.923445	32.58	211212A	17:32:25.512695	32.45	220316A	15:27:17.029072	20.86	220609D	19:10:18.018041	41.92
210908A	22:19:58.592099	31.81	211213A	13:45:06.586713	35.65	220316B	17:09:32.372506	44.54	220609E	21:01:11.088795	27.84
210909A	01:07:20.609274	31.55	211213B	13:52:01.498709	23.68	220317A	13:50:49.851166	18.43	220609F	22:59:25.952736	33.98
210909B	04:27:03.920394	21.76	211213C	16:54:41.883600	35.84	220318A	14:08:18.992087	32.90	220610A	17:19:54.832987	15.10
210909C	15:28:55.639208	30.78	211216A	11:16:58.593668	30.85	220318B	15:18:20.304462	33.22	220610B	18:28:43.994382	31.87
210909E	20:57:55.761237	16.58	211216B	13:39:53.280643	44.10	220318C	15:52:20.656472	20.03	220610C	19:57:59.998696	32.00
210910A	02:03:17.889358	28.54	211216C	15:55:58.400613	26.11	220318D	18:13:18.140876	39.81	220610D	22:15:13.201955	38.66
210910B	04:27:21.968835	20.86	211216E	17:02:09.504035	33.54	220319A	13:08:41.245958	22.40	220610E	23:17:43.299468	22.40
210910D	18:40:50.563266	24.51	211217A	18:29:40.080200	30.91	220319B	14:38:26.829850	36.74	220611A	02:59:30.559935	16.64
210910E	18:50:00.563266	36.29	211219A	12:25:25.424470	36.86	220319C	14:54:56.829850	31.42	220611B	11:59:33.249191	19.14
210910F	20:06:42.155830	32.38	211219B	18:09:03.457791	32.96	220319D	15:01:52.608670	42.37	220611C	16:33:51.644704	42.24
210910G	22:39:08.305256	21.63	211220A	07:02:10.937532	81.47	220319E	16:38:42.967615	22.08	220611D	18:33:17.544834	30.98
210911A	00:12:00.240242	18.69	211220B	13:48:31.676804	33.98	220319F	17:25:30.000122	32.64	220611E	21:25:54.191046	24.83
210911B	05:48:00.832587	39.10	211220C	14:03:16.480952	30.91	220319G	20:56:40.003168	27.46	220611F	23:03:21.916784	27.58
210911C	13:34:16.132285	18.69	211220D	16:56:59.998552	24.90	220320A	00:14:01.793261	14.08	220611G	23:27:24.524786	39.04
210911D	13:48:36.100282	28.61	211220E	20:02:06.544149	15.62	220320B	00:26:45.841260	16.90	220612A	01:23:03.537572	16.64
210911E	19:22:49.520966	19.78	211220F	20:08:47.952142	25.02	220320C	13:53:45.617518	41.41	220612B	03:08:19.184177	25.66
210911A	12:27:59.152865	30.78	211221A	01:11:57.872221	24.06	220320D	15:38:01.712649	28.22	220612C	07:10:27.232658	21.95
210912B	14:41:27.680692	39.55	211221B	12:23:52.272108	16.96	220320E	22:38:20.002102	28.22	220612D	13:07:28.243421	20.16
210912C	15:32:36.224096	27.65	211221C	13:31:17.168660	42.18	220321A	14:14:49.015956	21.18	220612F	17:02:48.288129	31.30
210912D	16:35:08.314202	45.57	211222A	03:02:17.424702	32.51	220321B	15:17:51.648315	28.29	220612G	17:51:36.389086	46.34
210912E	17:14:30.000114	34.30	211222B	10:12:32.880105	31.62	220321C	23:15:34.961617	54.98	220612H	18:31:24.832212	42.94
210912F	18:11:01.396202	15.94	211222D	13:14:06.487348	72.90	220322A	09:40:02.326979	28.99	220612I	19:06:32.192388	47.74
210912G	20:29:12.993005	25.92	211222F	14:51:01.418745	43.33	220322B	16:54:37.344510	22.59	220613A	14:34:06.202888	24.26

Table 10 continued on next page

Table 10 (*continued*)

Can.ID	Start of $T_{90,F}$ (UTC)	$T_{90,F}$ (s)	Can.ID (UTC)	Start of $T_{90,F}$ (UTC)	$T_{90,F}$ (s)	Can.ID (UTC)	Start of $T_{90,F}$ (UTC)	$T_{90,F}$ (s)	Can.ID (UTC)	Start of $T_{90,F}$ (UTC)	$T_{90,F}$ (s)
210912H	21:18:22.623608	41.86	211223A	04:43:08.119781	79.68	220323A	07:20:51.859942	21.38	220613B	16:40:26.640179	32.90
210913B	17:11:42.544031	27.26	211223B	06:52:32.298374	83.90	220323B	13:21:47.232014	32.70	220613C	19:38:08.727886	21.89
210914A	02:22:27.808460	32.13	211224A	09:29:21.169690	38.21	220323C	15:22:33.992002	26.05	220613D	20:27:38.816521	32.32
210914C	15:06:27.584895	25.54	211224B	14:53:28.720240	20.29	220323D	19:02:26.145088	28.74	220614A	15:57:38.616877	30.85
210915A	16:44:57.488213	29.57	211225A	20:56:31.024863	20.48	220323E	19:25:35.329099	4.61	220614B	19:04:27.675967	29.25
210916A	17:24:18.382941	50.75	211225B	22:03:22.816349	30.08	220324A	04:23:15.824822	34.11	220614C	19:43:26.793972	22.08
210917A	10:25:25.948020	23.10	211226A	04:02:32.665645	65.92	220324B	12:39:29.696255	50.24	220615A	02:26:27.345209	28.54
210917B	13:54:04.127080	30.27	211226B	07:29:05.427837	32.90	220324C	19:17:04.801007	25.60	220615B	13:55:15.749186	26.50
210918A	00:07:51.456721	28.48	211226F	21:24:14.864020	25.54	220324D	23:19:19.504147	22.40	220615C	15:58:23.872464	21.89
210918B	04:39:35.681021	29.44	211226G	22:48:11.267709	19.26	220325A	08:21:05.101908	28.93	220615D	18:25:07.680192	24.64
210918C	05:05:59.600567	30.34	211227B	10:37:54.545321	19.26	220325B	10:00:12.997992	39.04	220615E	18:26:07.144015	25.79
210918D	10:08:46.106535	33.86	211228A	08:03:42.672050	25.73	220326A	07:25:23.808305	16.13	220616A	04:59:12.960250	21.44
210918E	13:58:10.624110	44.03	211228B	12:00:50.001496	35.46	220326B	07:26:37.008299	16.38	220616B	06:12:05.778202	32.58
210918F	15:11:32.527451	32.13	211229A	15:03:19.680303	30.02	220326C	08:13:19.047482	15.62	220616D	18:38:16.205141	22.78
210918G	15:41:41.935459	28.93	211229B	16:28:57.698478	20.93	220326D	08:20:33.287481	18.18	220617A	03:37:51.280353	38.66
210918H	17:53:23.088164	28.99	211229C	21:57:32.767341	18.75	220326E	08:22:30.391482	14.40	220618A	00:11:02.736008	32.19
210919A	03:41:27.600409	28.10	211229D	22:26:30.000620	42.43	220326G	08:34:20.439490	14.14	220618B	16:29:16.094950	48.64
210919B	14:48:15.150024	39.04	211229E	22:43:18.688623	25.09	220326H	08:43:50.343494	15.23	220618C	17:45:07.992015	26.94
210919C	16:49:12.363583	23.49	211230A	06:29:37.626934	23.10	220327A	06:53:48.271576	19.52	220619A	02:06:23.042068	34.24
210919D	23:44:16.992575	42.94	211230B	09:21:18.468127	32.06	220327B	08:38:29.408320	16.45	220619B	13:26:19.600452	21.82
210920A	03:51:40.385231	24.26	211230C	10:58:10.112932	46.66	220327C	12:03:04.480136	35.46	220619C	14:36:29.800470	41.22
210920B	04:34:04.184494	45.25	211230D	13:39:52.604577	29.31	220327D	12:26:53.712136	22.98	220619D	20:46:01.312348	19.39
210920C	11:19:24.530248	59.65	211231A	01:15:23.595765	77.95	220327E	13:58:33.984690	37.76	220619E	23:25:01.664021	23.68
210920D	13:08:24.912018	34.69	211231B	10:01:34.032561	27.07	220327F	19:46:20.384017	27.26	220620A	04:05:54.113518	18.24
210921A	07:43:34.250956	31.04	211231C	15:20:17.585269	25.92	220328A	11:24:52.449072	40.13	220620B	11:18:47.306357	21.57
210921B	09:44:10.827337	34.11	211231D	19:55:00.672918	23.23	220328C	21:12:56.192085	25.60	220620C	12:49:06.828976	29.44
210921C	11:01:56.787444	40.32	211231E	22:39:07.728750	22.21	220329A	02:03:16.064380	23.87	220620D	15:21:06.112535	32.26
210921D	11:27:36.787444	30.46	220101A	02:46:20.557006	37.76	220329C	13:18:10.002784	37.25	220620E	19:26:59.157611	28.42
210921E	14:29:03.124513	22.40	220101B	06:17:58.334167	22.59	220329F	21:21:16.289390	25.60	220621A	04:17:07.552296	36.29
210921F	19:06:33.056148	23.42	220101C	07:42:03.606148	31.68	220329G	22:02:54.496142	45.44	220621B	11:04:53.522402	36.42
210921G	23:18:33.796602	46.14	220101D	15:58:38.592370	25.34	220329H	22:46:26.784138	35.26	220621C	20:45:19.728083	16.19
210922A	10:54:08.660979	43.39	220101E	21:51:59.088786	15.55	220329I	22:54:24.864144	35.07	220621D	21:07:20.240746	33.73
210922B	10:57:42.047699	52.54	220102A	03:38:47.912016	25.02	220330A	02:57:37.361548	20.93	220622A	02:32:50.000030	43.65
210922C	14:34:38.739387	34.75	220102B	05:58:00.000852	55.81	220330B	04:36:48.560147	26.82	220622B	03:21:50.000338	40.90

Table 10 *continued on next page*

Table 10 (continued)

Can.ID	Start of $T_{90,F}$ (UTC)	$T_{90,F}$ (s)	Can.ID (UTC)	Start of $T_{90,F}$ (UTC)	$T_{90,F}$ (s)	Can.ID (UTC)	Start of $T_{90,F}$ (UTC)	$T_{90,F}$ (s)	Can.ID (UTC)	Start of $T_{90,F}$ (UTC)	$T_{90,F}$
210922D	14:39:02.499376	20.86	220102C	11:14:30.002228	39.04	220330C	12:15:07.405201	36.16	220622C	12:13:47.864126	37.18
210922E	19:03:33.893003	34.88	220102D	11:33:00.002228	27.84	220330D	12:58:52.225413	53.89	220622D	13:27:01.776093	28.16
210923A	08:27:05.937690	24.00	220102E	12:06:48.004058	31.94	220331A	07:56:02.256440	47.68	220622E	14:15:24.721185	25.02
210923B	09:34:18.032395	30.85	220102F	15:21:25.248036	22.72	220331B	09:49:05.875610	24.06	220622F	16:27:01.776697	28.16
210923C	09:58:00.000208	30.91	220102G	19:39:45.120514	34.82	220331C	10:22:05.492717	18.24	220622G	16:47:49.648685	30.34
210923D	12:20:11.487852	31.10	220103A	04:12:40.000070	37.18	220401A	03:25:33.872007	80.06	220622H	19:35:14.752766	39.10
210923E	12:33:04.431852	16.13	220103B	04:59:53.347041	6.59	220401B	06:43:35.000000	44.80	220623A	12:01:53.569702	27.46
210923F	13:52:36.998984	25.15	220103C	05:32:24.000000	34.24	220401C	14:17:45.056252	20.80	220623B	12:03:30.001700	23.74
210924A	09:06:57.632710	18.94	220103D	07:53:44.522971	23.17	220401D	22:27:46.625570	28.10	220623C	13:36:49.000000	35.39
210924B	10:39:08.643981	26.30	220103E	10:53:41.557796	35.26	220401E	22:45:44.113585	5.82	220623D	15:15:31.000000	27.26
210924C	12:06:11.706164	20.99	220104A	02:06:04.738762	40.06	220402A	07:46:05.928017	19.01	220623E	17:04:16.336240	57.41
210924D	17:42:45.360208	24.58	220104B	06:00:56.816193	24.70	220402B	17:42:29.312367	90.62	220624A	00:59:27.678466	32.26
210924E	19:14:55.905404	25.09	220104D	07:02:02.144502	23.04	220402C	17:44:30.128369	79.81	220624B	02:11:29.168328	34.62
210925A	11:51:39.064090	28.29	220104E	07:30:18.032509	41.02	220403A	06:31:31.374808	27.65	220624C	10:42:58.220903	21.06
210925B	15:57:18.239717	51.71	220104F	09:13:05.088090	29.57	220403B	16:53:37.953702	31.04	220624E	18:16:35.778199	16.58
210926A	10:58:40.512467	27.39	220104G	13:42:00.000466	21.25	220404A	07:47:03.729651	25.86	220626B	17:59:21.792783	38.14
210926B	11:36:34.519577	35.65	220105A	05:28:58.446560	28.29	220404B	09:23:24.987136	26.88	220626C	18:20:40.896777	37.89
210926C	15:44:15.265276	32.90	220105B	08:42:04.532993	19.78	220404D	14:32:34.082787	25.86	220626D	22:06:35.776704	44.16
210926D	21:05:30.673736	16.90	220105C	12:32:28.896941	21.82	220404F	19:43:10.593346	25.54	220627A	00:19:34.864466	35.07
210926E	21:22:20.641739	23.62	220105D	22:14:25.472007	78.46	220405A	17:16:50.145299	45.12	220627B	01:57:51.744092	22.34
210927A	08:23:02.340068	29.89	220106A	11:15:00.529567	20.42	220406A	05:34:47.000000	38.34	220627C	10:38:37.448014	31.49
210927B	16:56:53.681346	24.13	220106B	15:28:41.217189	38.72	220407A	08:51:22.826475	33.22	220627D	11:51:54.344370	25.60
210929A	01:44:35.361726	16.32	220107A	02:25:15.104232	24.83	220407B	09:26:56.784008	43.01	220627E	12:20:27.120017	18.82
210929B	04:25:07.669154	29.12	220107B	05:02:51.296466	20.67	220407C	22:30:13.416007	75.52	220627F	13:01:13.328260	36.61
210929C	22:05:20.368966	35.46	220107C	09:51:57.4444580	30.40	220408A	00:10:34.656008	73.28	220627G	21:23:40.000472	22.72
210930A	16:41:10.000192	36.03	220108A	02:53:38.184525	39.68	220408B	04:35:49.696683	32.00	220628A	01:22:33.969807	22.02
210930B	19:40:05.248231	24.13	220108B	03:47:41.072022	25.66	220408C	06:45:58.000000	33.22	220628B	12:33:45.456707	41.47
211001A	01:40:56.514250	23.42	220108C	05:08:23.344294	32.90	220408D	08:24:21.000000	25.60	220628C	19:50:24.961643	31.36
211001B	07:34:54.557865	30.27	220108D	11:48:55.568034	24.83	220410A	04:50:49.753311	22.14	220629A	06:04:30.482628	31.36
211001C	08:54:09.969168	25.15	220108E	14:12:24.402517	25.54	220410B	21:49:38.072006	84.86	220629B	06:12:06.866631	28.67
211001D	13:22:24.481718	35.46	220109B	11:41:29.747305	25.98	220411A	01:18:58.083668	21.12	220629C	08:56:50.999708	50.43
211002A	10:32:40.147606	47.30	220109C	21:21:21.368006	85.57	220411B	06:56:13.401720	22.85	220629D	21:59:25.629624	34.30
211002B	17:33:50.000034	45.82	220110A	13:04:24.724663	26.69	220411C	12:34:10.384217	27.26	220629E	22:37:51.728557	38.21
211003A	12:41:57.105158	16.51	220110B	15:29:05.920386	14.02	220412A	06:26:00.976085	21.06	220630A	03:46:56.053822	24.70

Table 10 continued on next page

Table 10 (*continued*)

Can.ID	Start of $T_{90,F}$ (UTC)	$T_{90,F}$ (s)									
211004A	04:56:28.668496	32.13	220110C	15:38:07.104386	42.88	220412B	08:21:15.712376	44.22	220630B	05:42:16.311540	23.94
211004B	07:26:48.880125	36.54	220111A	02:36:37.922229	32.83	220412C	13:17:32.704596	27.46	220630C	07:09:46.101652	31.49
211004C	11:48:18.656308	28.35	220111B	07:29:16.161167	3.78	220412D	16:36:30.000510	40.77	220630D	11:24:26.274214	22.78
211005A	01:23:43.177128	22.59	220111C	15:57:50.592144	29.38	220412E	21:29:03.186406	26.94	220630E	13:55:56.992727	29.44
211005B	03:17:38.240047	35.52	220111D	19:14:23.224007	75.71	220412F	21:45:33.186406	26.11	220630F	14:32:02.208110	34.88
211005C	03:24:01.168056	35.20	220112A	01:51:27.000000	38.59	220414A	02:23:24.378510	36.67	220630G	19:54:50.002702	33.09

NOTE— (This table is available in its entirety in machine-readable form.)